

System Identification Based on Deconvolution and Cross Correlation: An Application to a 20-Story Instrumented Building in Anchorage, Alaska

by Weiping Wen and Erol Kalkan

Abstract Deconvolution and cross-correlation techniques are used for system identification of a 20-story steel, moment-resisting frame building in downtown Anchorage, Alaska. This regular-plan midrise structure is instrumented with a 32-channel accelerometer array at 10 levels. The impulse response functions (IRFs) and correlation functions (CFs) are computed based on waveforms recorded from ambient vibrations and five local and regional earthquakes. The earthquakes occurred from 2005 to 2014 with moment magnitudes between 4.7 and 6.2 over a range of azimuths at epicenter distances of 13.3–183 km. The building's fundamental frequencies and mode shapes are determined using a complex mode indicator function based on singular value decomposition of multiple reference frequency-response functions. The traveling waves, identified in IRFs with a virtual source at the roof, and CFs are used to estimate the intrinsic attenuation associated with the fundamental modes and shear-wave velocity in the building. Although the cross correlation of the waveforms at various levels with the corresponding waveform at the first floor provides more complicated wave propagation than that from the deconvolution with virtual source at the roof, the shear-wave velocities identified by both techniques are consistent—the largest difference in average values is within 8%. The median shear-wave velocity from the IRFs of five earthquakes is 191 m/s for the east–west (E-W), 205 m/s for the north–south (N-S), and 176 m/s for the torsional responses. The building's average intrinsic-damping ratio is estimated to be 3.7% and 3.4% in the 0.2–1 Hz frequency band for the E-W and N-S directions, respectively. These results are intended to serve as reference for the undamaged condition of the building, which may be used for tracking changes in structural integrity during and after future earthquakes.

Introduction

Wave propagation in buildings can be used for tracking the changes in buildings' stiffness, which is a primary goal of structural health monitoring. Cross correlation, deconvolution, and cross coherence are effective to extract the Green's functions, which account for wave propagation between receivers (Snieder *et al.*, 2009; Wapenaar *et al.*, 2010). Among them, the deconvolution has been used widely for computing shear-wave propagation in buildings. This method is appealing because it considers correlation of motions at different observation points and changes the boundary condition at the base. The structural response can be recovered using impulse response functions (IRFs) regardless of its coupling to the subsurface (Snieder and Şafak, 2006; Vasconcelos and Snieder, 2008) provided that no rocking takes place at the foundation level (Todorovska, 2009; Ebrahimian and Todorovska, 2014, 2015; Rahmani *et al.*,

2015a). This method was applied to earthquake shaking (e.g., Snieder and Şafak, 2006; Kohler *et al.*, 2007; Todorovska and Trifunac, 2008; Picozzi *et al.*, 2011; Newton and Snieder, 2012; Picozzi, 2012; Todorovska and Rahmani, 2012; Nakata *et al.*, 2013; Rahmani and Todorovska, 2013; Cheng *et al.*, 2015; Petrovic and Parolai, 2016) and ambient-vibration data (Prieto *et al.*, 2010; Nakata and Snieder, 2014) to retrieve the velocity of traveling shear waves and intrinsic attenuation in buildings instrumented with accelerometer arrays. It was also applied to borehole strong-motion data (e.g., Mehta *et al.*, 2007a,b; Parolai *et al.*, 2009, 2010; Oth *et al.*, 2011; E. Kalkan *et al.*, unpublished manuscript, 2017; see [Data and Resources](#)) to examine wave propagation in the shallow geological layers.

Two other techniques, cross correlation (Schuster *et al.*, 2004; Larose *et al.*, 2006; Schuster, 2009) and cross coher-



Figure 1. Photo showing north façade of the 20-story-high Atwood Building next to the Delaney Park borehole array (fenced area) in downtown Anchorage, Alaska. Google map shows the location of Delaney Park (photograph by E. Kalkan). The color version of this figure is available only in the electronic edition.

ence (Aki, 1957), are broadly used in various seismological applications including surface-wave tomography based on ambient noise, and creating virtual sources for improved reflection for regional and global explorations. In contrast to deconvolution, cross correlation depends on the incoming wave and the ground coupling. Because of this reason, its application to data from instrumented buildings is limited (Nakata *et al.*, 2013).

In this study, we applied deconvolution and cross correlation to earthquake-shaking and ambient-vibration data from an instrumented building to extract the building dynamic characteristics and monitor the changes in those characteristics over time. The structure selected (Robert B. Atwood Building) is a 20-story, steel-moment frame office building located in Anchorage, Alaska. The U.S. Geological Survey's Advanced National Seismic System furnished this building with a 32-channel accelerometer array at 10 levels in 2003. The building's instrumentation is accompanied by a free-field station and downhole array located in Delaney Park, 180 m away from the building, to measure soft sediments' response to earthquake shaking, and to provide input

wavefield data for the structure. Figure 1 shows the photo and map view of the Atwood Building and nearby Delaney Park geotechnical array.

Since 2003, more than a dozen earthquakes with moment magnitude (M) 4.5 and above have been recorded in the building. Yang *et al.* (2004) applied spectral ratios of basement and roof motions from ambient vibration and from a local event (12 December 2003 local magnitude 3.7) to compute the modal frequencies in north–south (N–S) and east–west (E–W) directions of the building. Çelebi (2006) used data from three earthquakes with low-amplitude motions (8 November 2004 M 4.9, 16 February 2005 M 4.7, and 6 April 2005 M 4.9) to identify modal frequencies based on the same approach, and modal-damping values using the procedure in Ghanem and Shinozouka (1995). In this study, we used both earthquake-shaking data from five local and regional events and ambient-vibration data to identify the traveling waves in the IRFs with a virtual source at the roof, and correlation functions (CFs) to determine the intrinsic attenuation associated with the fundamental modes and to compute shear-wave velocity in the building. The shear-

Table 1

List of Abbreviations and Symbols Present in This Article

BCF	Bootlegger Cove Formation
c	Wave velocity
C	Cross-correlation vector
CF	Correlation function
CMIF	Complex mode indicator function
D	Deconvolution vector
E-W	East–west
f	Frequency
FRF	Frequency response function
h	Traveling distance of wave
h_{\min}	Minimum layer height
H	Building's total height
i	Imaginary unit
IRF	Impulse response function
k	Wavenumber
L	Wave travel distance
M	Moment magnitude
MAC	Modal assurance criterion
$n\text{RMSD}$	Normalized root mean square deviation
N_0	Number of degrees of freedom
N-S	North–south
Q	Quality factor
P_{xx}	Power spectral density
P_{xy}	Cross power spectral density
r	Reflection coefficient in time domain
R	Reflection coefficient in frequency domain
RMSD	Root mean square deviation
s	Excitation source at fixed base in time domain
S	Excitation source at fixed base in frequency domain
T	Time instant
u	Response
\hat{u}	Predicted value of observed floor displacement
u_{\max}	Maximum absolute value of the observed floor displacement
u_{\min}	Minimum absolute value of the observed floor displacement
USGS	U.S. Geological Survey
V_S	Shear-wave velocity
z	Height
ε	Regularization parameter
ω	Circular frequency
ξ	Damping ratio
τ	Wave travel time
ϕ_{mgr}	Coefficient for degree-of-freedom q and mode r of m th excitation

wave velocity is a good indicator of nonlinearity because it is directly related to the structural rigidity, and its decrease signifies change in stiffness conceivably initiated by damage (Kawakami and Oyunchimeg, 2004; Todorovska and Trifunac, 2008; Ulusoy *et al.*, 2013; Ebrahimian and Todorovska, 2015; Nakata *et al.*, 2015; Rahmani and Todorovska, 2015; Rahmani *et al.*, 2015a,b).

The results of this full-scale case study not only confirm the robustness of the wave method for system identification of instrumented buildings, but also serve as a reference for the undamaged condition of the Atwood Building for tracking changes in its structural integrity during and after future earthquakes.

The list of abbreviations and symbols used throughout this article is given in Table 1.

Tectonic Setting and Geology

Anchorage, Alaska, lies within one of the most active tectonic environments, and thus has been subjected to recurrent seismic activity. The city is erected on the edge of a deep sedimentary basin in the upper Cook Inlet region surrounded by the Bruin Bay–Castle Mountain fault system in the west, the Border Ranges fault system in the east, and the Knik fault along the west front of the Chugach Mountains (Lade *et al.*, 1988). Most of the regional seismicity can be attributed to underthrusting along the Benioff zone of the plate boundary megathrust (Li *et al.*, 2013). The Benioff zone dips to the northwest beneath the Cook Inlet region (Fogelman *et al.*, 1978; Plafker *et al.*, 1994). Large historical earthquakes have ruptured along much of the length of this megathrust (Wong *et al.*, 2010).

The Paleogene strike slip along the Border Ranges fault was transferred to dextral slip on the Castle Mountain fault through a complex fault array in the Matanuska Valley and strike-slip duplex systems in the northern Chugach Mountains (Smart *et al.*, 1996). There is some evidence suggesting that both the Castle Mountain (Bruhn, 1979; Lahr *et al.*, 1986) and Border Ranges fault systems (Udike and Ulery, 1986) may be active and capable of propagating moderate-size earthquakes. The strike-slip Castle Mountain fault approaches to within about 40 km of Anchorage. Each year, earthquakes with M above 4.5 are felt in the city as a result of this seismic setting (Boore, 2004).

The geological section at the Atwood Building site consists of glacial outwash, overlying Bootlegger Cove formation (BCF), and glacial till deposited in a late Pleistocene glaciomarine–glaciodeltaic environment (14,000–18,000 years ago) (Ulery and Udike, 1983). The glacial outwash contains gravel, sand, and silt, commonly stratified, deposited by glacial melt water. This surficial mud layer of soft estuarine silts overlays an ~35-m-thick glacioestuarine deposit of stiff to hard clays with interbedded lenses of silt and sand; this glacioestuarine material is known locally as the BCF. Underlying the BCF is a glaciofluvial deposit from the early Naptowne glaciation (Udike and Carpenter, 1986) consisting mainly of dense to very dense sands and gravels with interbedded layers of hard clay (Finno and Zapata-Medina, 2014).

The BCF (from 20 to 50 m) has major facies with highly variable physical properties (Udike and Ulery, 1986). Cone penetration test blow counts are down in the single digits at depths of over 30 m in BCF, and shear-wave velocity diminishes with depth through this formation (Steidl, 2006). The glacial till is composed of unsorted, nonstratified glacial drift consisting of clay, silt, sand, and boulders transported and deposited by glacial ice. The relatively thin (<12.5 m) glacial outwash at the surface is locally underlain by sensitive facies of the BCF that could cause catastrophic failures

during earthquakes, as occurred during the Great Alaskan earthquake (also known as Prince William Sound earthquake) with M 9.2 on 27 March 1964.

Because of the lack of *in situ* measurements, the shear-wave velocity (V_S) of the soil column was estimated by [Nath et al. \(1997\)](#) and [Yang et al. \(2008\)](#) from inversion of data at a nearby site, about 200 m away from the Atwood Building (U. Dutta, University of Alaska, Anchorage, oral comm., 2014). The measurements show that the V_S increases initially within the glacial outwash at shallower depths, and then decreases within the deeper BCF (Fig. 2). The average V_S within the first 30 m of surface is 250 m/s, corresponding to National Earthquake Hazards Reduction Program site class D (stiff soil).

The Building, Instrumentation, and Data

The Atwood Building, located at northwest downtown Anchorage, Alaska, is a 20-story, moment-resisting steel frame office structure with a basement used as a parking garage (Fig. 3a). The building was designed according to the 1979 Uniform Building Code ([International Conference of Building Officials \[ICBO\], 1979](#)), and constructed in 1980. It has a square footprint of 39.6 m (130 ft) with a square concrete core of 14.6 m (60 ft) (Fig. 3b). The total height of the building is 80.54 m (264.2 ft). The building's reinforced concrete shallow foundation consists of a 1.52-m (5 ft) thick mat under the center core with a perimeter wall footing connected with grade beams (Fig. 3c).

The instrumentation consists of a 24-bit IP-based Kinematics Granite data logger and an array of 32 accelerometers distributed on 10 levels (Fig. 4): basement, 1st (ground), 2nd, 7th, 8th, 13th, 14th, 19th, 20th, and roof. Among the sensors, 29 of them are 2g-uniaxial (Kinematics ES-U) and one tri-axial Force Balance Accelerometers (Kinematics ES-T) with 1.25 V/g sensitivity. The ES-T (channels 1–3) is located at the northwest corner of the basement to measure the three orthogonal components of ground motion. Two vertically oriented accelerometers (channels 4 and 6) are located in the basement at the southwest and northeast corners to compute the rocking motion of the building. The rest of the 27 accelerometers were placed on nine different floors to measure the building's lateral motions along the E-W and N-S directions, and to compute its torsional motions. The relative floor displacements (story drifts) can be computed using the recorded accelerations at the same corners of the building. This accelerometer array records 200 samples per second data in real time; data are stored on a ring buffer of the data logger. The ring buffer is large enough to save a week of continuous waveforms.

More than a dozen earthquakes with M 4.5 and above have been recorded with no signs of damage since the deployment of the building's instrumentation array. Five earthquakes with M between 4.5 and 6.2 were identified for this study based on their proximity to the building and intensity of recordings. Other distant small-magnitude earthquakes

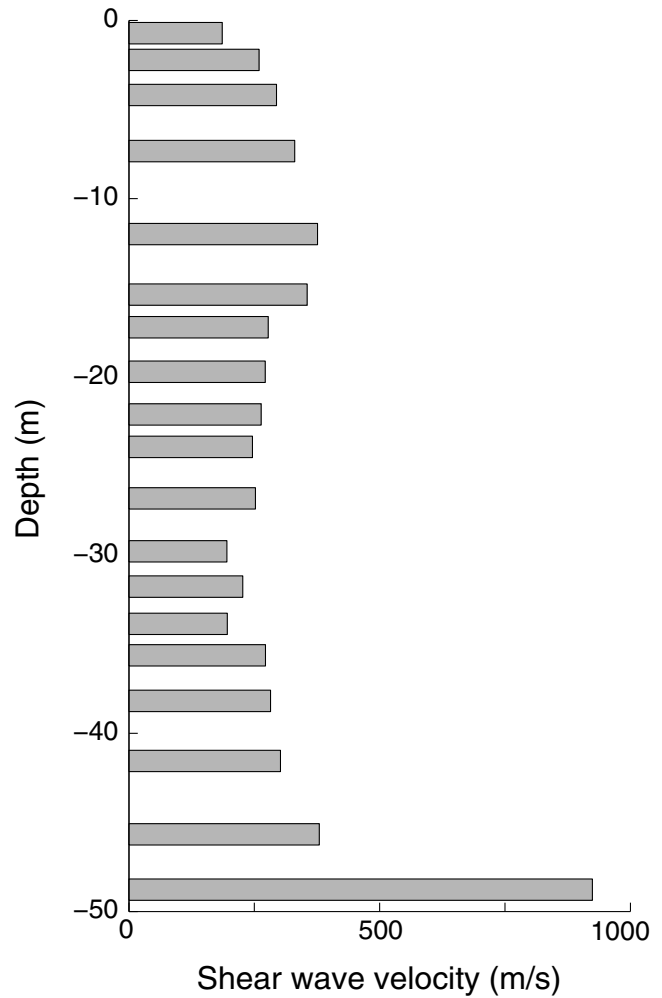


Figure 2. Shear-wave velocity with depth based on geophysical measurements at a site about 200 m away from the Atwood Building (adapted from [Nath et al., 1997](#), and [Yang et al., 2008](#)). Shear-wave velocity is lower between –20 and –48 m at Bootlegger Cove formation than the shallower glacial outwash (between 0 and –12.2 m).

were discarded due to the low signal-to-noise ratio of their waveforms. The events selected are listed in Table 2 along with origin times, magnitudes, distance, depth, and epicenter coordinates. The epicenters of those events are depicted on a regional map in Figure 5; the known active faults in the vicinity of Anchorage are also shown in this map. Events selected are 17–102.8 km deep. Figure 6 compares horizontal accelerations recorded at the first floor with those at the roof level during five earthquakes. The largest peak acceleration of 15%g was recorded at the roof level during the 25 September 2014 (M 6.2) event at an epicenter distance of 102.1 km. Figure 7 shows the full waveforms in the building's reference E-W direction obtained from this event; the waveforms from the basement amplified as much as 3.4 times at the roof level due to the building's response. In addition to the earthquake-shaking data, about 17 min (1014 s) of ambient-vibration data obtained on 13 December 2003 are analyzed.

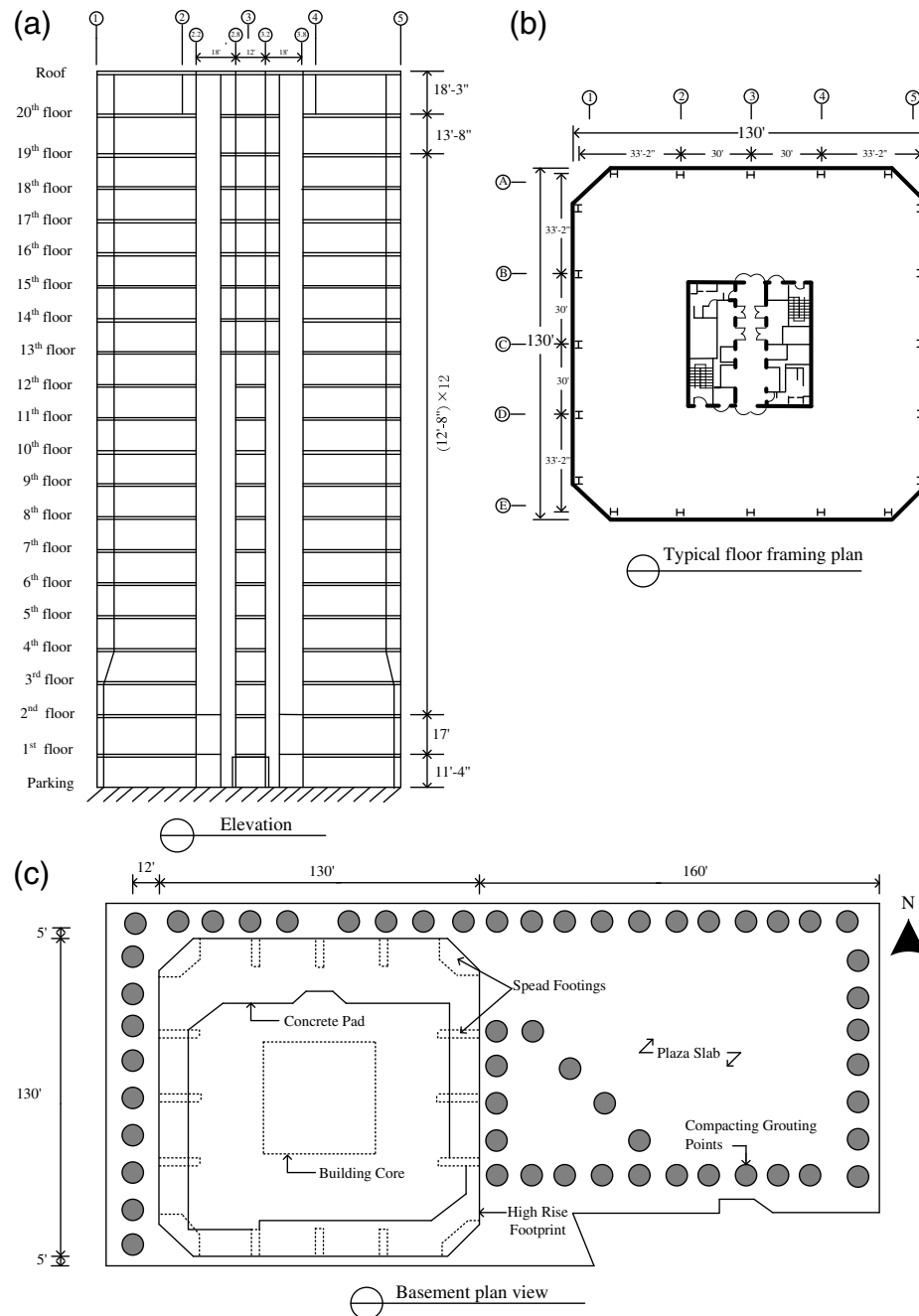


Figure 3. (a) Elevation, (b) typical floor plan, and (c) basement plan of the Atwood Building; units are in feet and inches.

Table 2

Origin Times, Magnitudes, Epicenter Locations of Local and Regional Earthquakes Recorded by the Atwood Building Accelerometer Array in Anchorage, Alaska, between 2005 and 2014

Event	Origin Time (UTC) (yyyy/mm/dd hh:mm:ss)	Moment Magnitude	Epicenter Coordinates			Epicenter Distance (km)	Peak Acceleration (cm/s ²)	
			Latitude (°)	Longitude (°)	Depth (km)		Ground	Structure
1	2005/04/06 17:51:36	4.9	61.454	-146.518	17.0	183.0	8.1	13.7
2	2006/07/27 06:42:37	4.7	61.155	-149.678	36.0	13.3	24.3	41.8
3	2009/06/22 11:28:05	5.4	61.939	-150.704	64.6	89.4	7.9	18.6
4	2010/09/20 13:44:02	4.9	61.115	-150.219	45.4	20.7	22.8	38.1
5	2014/09/25 09:51:17	6.2	61.950	-151.790	102.8	102.1	71.6	147.1

The earthquakes are numbered sequentially according to their origin times. Peak acceleration is the observed absolute maximum amplitude of the waveforms from the accelerometers at the ground and roof floors.

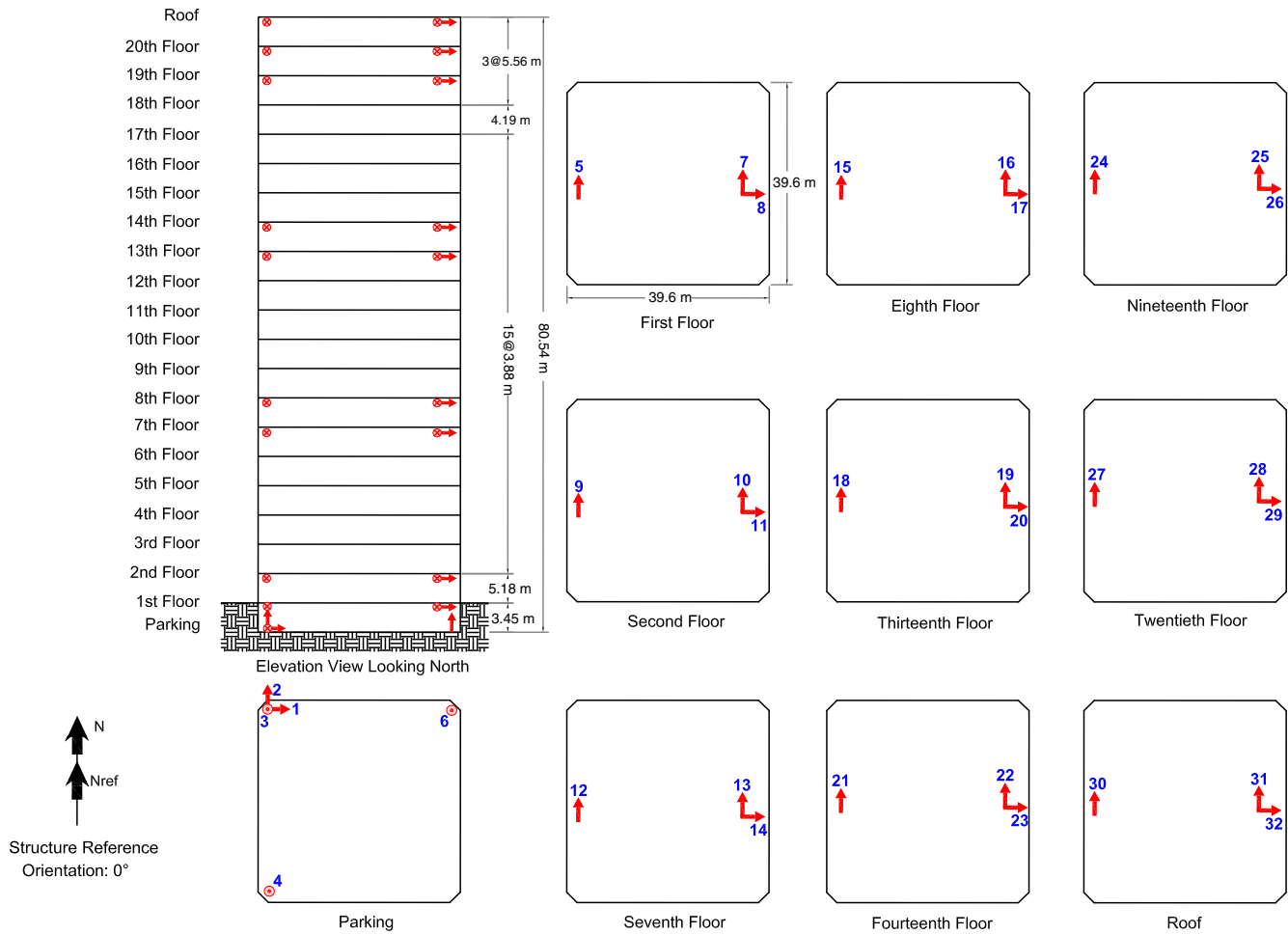


Figure 4. Instrumentation layout of the Atwood Building; arrows indicate sensor orientation; numbers indicate sensor IDs. Height of each floor and total height of the building from the ground level are shown (see [Data and Resources](#)). The color version of this figure is available only in the electronic edition.

Seismic Interferometry

In the time domain, the total response considering the 1D wave propagation in an elastic fixed-base shear column, similar to the shear-beam model proposed by [Iwan \(1997\)](#), can be formulated as

$$\begin{aligned}
 u(t, z) = & A(t, z)s\left(t - \frac{z}{c}\right) + A(t, 2H - z)s\left(t - \frac{2H - z}{c}\right) \\
 & + r(t)A(t, 2H + z)s\left(t - \frac{2H + z}{c}\right) \\
 & + r(t)A(t, 4H - z)s\left(t - \frac{4H - z}{c}\right) \dots, \quad (1)
 \end{aligned}$$

in which $u(t, z)$ is the response at height z ($z = 0$ at the base), $s(t)$ is the excitation source at the fixed base, H is the total height, c is the traveling shear-wave velocity, and $r(t)$ is the reflection operator. The attenuation occurs during wave propagation when a wave travels over a distance L , which is described by attenuation operator $A(t, L)$. For a constant

Q model, this attenuation operator in frequency domain is given by [Aki and Richards \(2002\)](#):

$$A(\omega, L) = \exp(-\xi|\omega|L/c), \quad (2)$$

in which ω is the cyclic frequency defined as $2\pi/t$ and ξ is the viscous-damping ratio related to Q as $\xi = 1/2Q$. Equation (1) shows that the response is the summation of an infinite number of the upward and downward traveling waves. The first term is the upward traveling wave, and the second term represents the reflection of the first wave at the roof (free end) and travels downward. This wave reflects off the fixed base and travels upward, which is the third term. The last term is the reflection of the third wave at the roof, which travels downward. The response in the frequency domain is

$$\begin{aligned}
 u(\omega, z) = & \sum_{n=0}^{\infty} S(\omega)R^n(\omega)\{e^{ik(2nH+z)}e^{-\xi k(2nH+z)} \\
 & + e^{ik(2(n+1)H-z)}e^{-\xi k(2(n+1)H-z)}\}, \quad (3)
 \end{aligned}$$

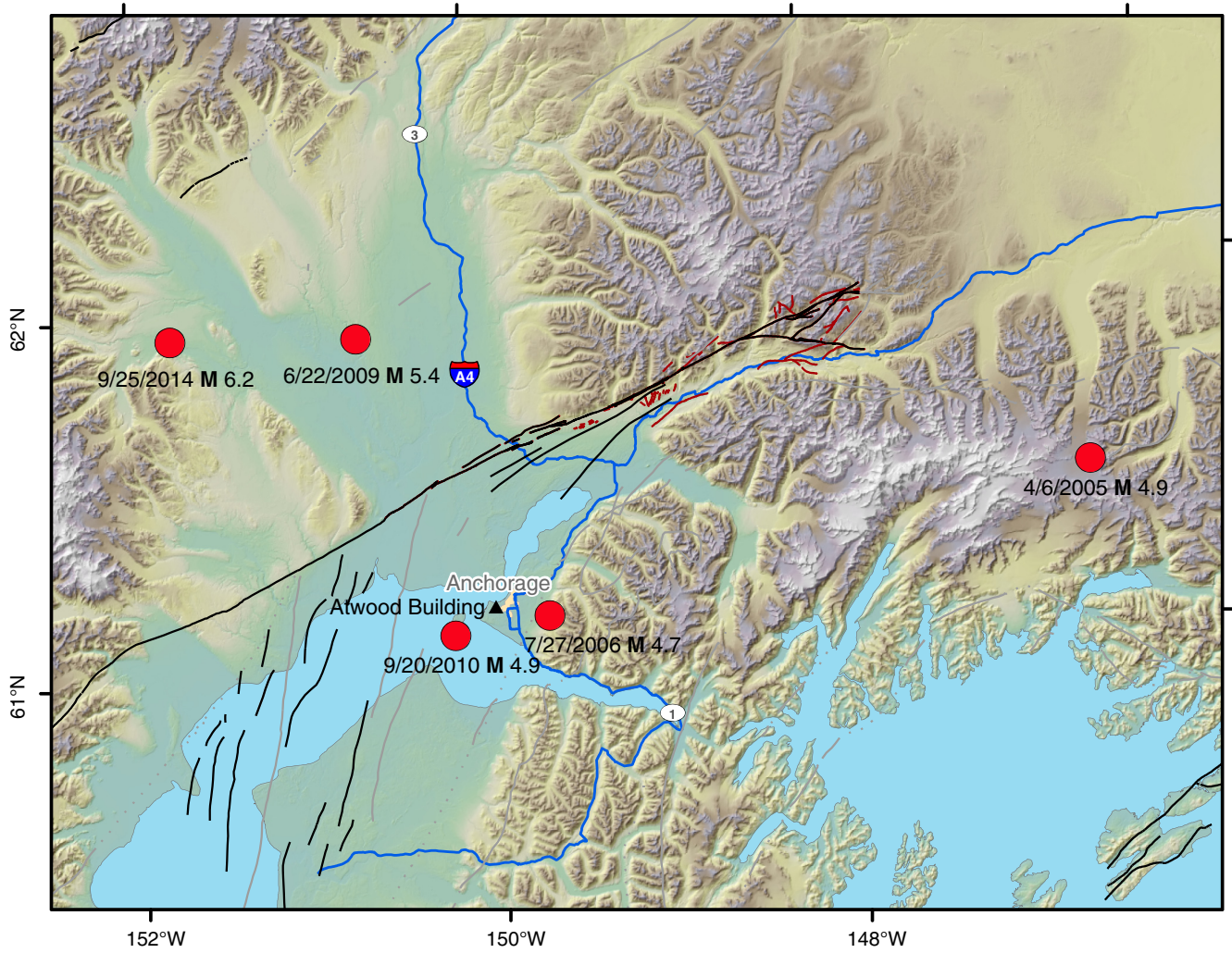


Figure 5. Map showing location of the Atwood Building by triangle (61.21528° N and 149.89296° W) and epicenters of selected five earthquakes with circles (summarized in Table 1); quaternary faults and major highways are indicated in and around Anchorage, Alaska (M, moment magnitude; see Data and Resources). The color version of this figure is available only in the electronic edition.

in which $k = \omega/c$ is the wavenumber, i is the imaginary unit, $S(\omega)$ is the source excitation, and $R(\omega)$ is the reflection coefficient. The formulation for deconvolution and cross correlation can be derived using equation (3).

Deconvolution

The deconvolution of the response at height z , $u(z, \omega)$ by the response at height z_a , $u(z_a, \omega)$ is defined as

$$D(z, z_a, \omega) = u(z, \omega) / u(z_a, \omega). \quad (4)$$

The above equation may become ill conditioned when the denominator approaches zero. Thus, the following regularized format is used as the estimator of deconvolution:

$$D(z, z_a, \omega) = [u(z, \omega) u^*(z_a, \omega)] / [|u(z_a, \omega)|^2 + \varepsilon \langle |u(z_a, \omega)|^2 \rangle], \quad (5)$$

in which superscript $*$ denotes the complex conjugate, ε is the regularization parameter ($\varepsilon = 0.01$ is used here), and $\langle |u(z_a, \omega)|^2 \rangle$ is the average power spectrum of $u(z_a, \omega)$.

By plugging equation (3) into equation (4) and making appropriate cancellations of incoming wave $S(\omega)$ and the reflection coefficient $R(\omega)$, the deconvolution $D(z, z_a, \omega)$ can be obtained as

$$D(z, z_a, \omega) = \sum_{n=0}^{\infty} (-1)^n \{ e^{ik(2n(H-z_a)+z-z_a)} e^{-\xi k(2n(H-z_a)+z-z_a)} + e^{ik(2n(H-z_a)+2H-z-z_a)} e^{-\xi k(2n(H-z_a)+2H-z-z_a)} \} \quad (6)$$

(Nakata *et al.*, 2013). The incoming wave $S(\omega)$ and the reflection coefficient $R(\omega)$ are not present in the analytical expression of the deconvolution, and thus deconvolution can remove the influences of $S(\omega)$ and $R(\omega)$. Todorovska

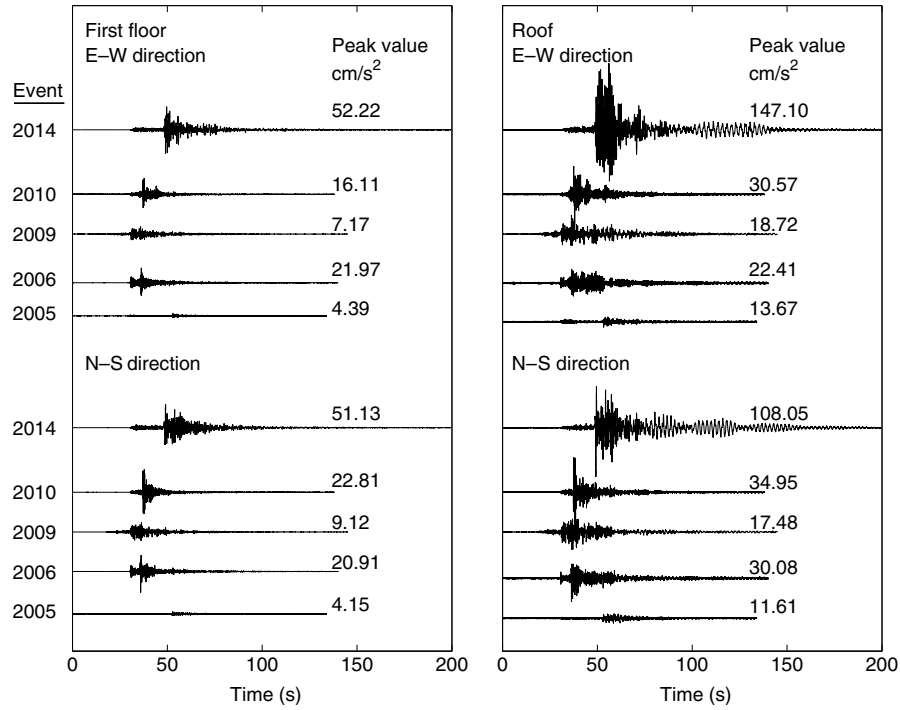


Figure 6. Horizontal acceleration waveforms recorded at first floor and roof level during five earthquakes summarized in Table 1.

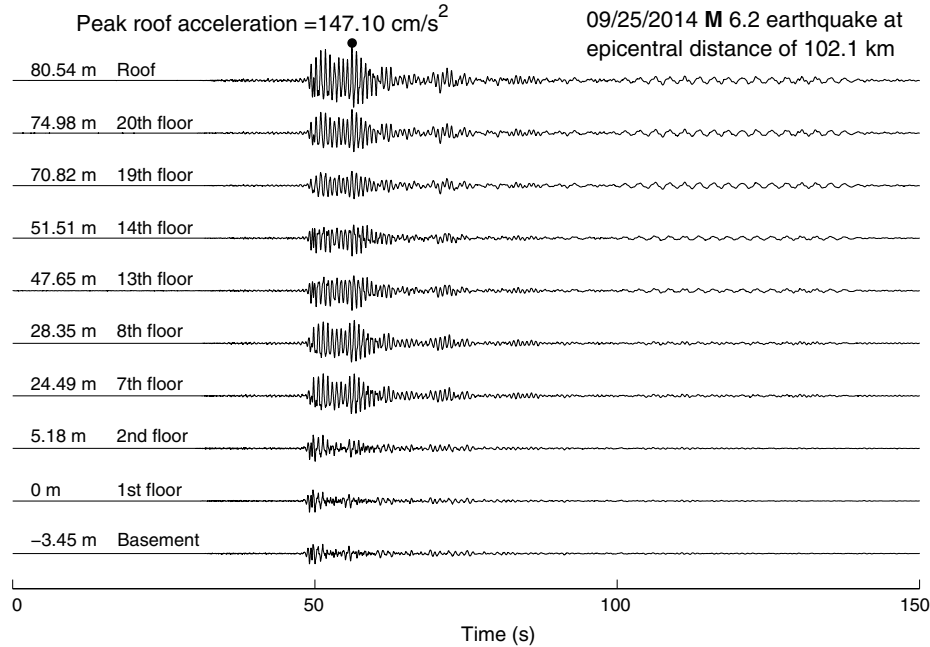


Figure 7. East-west (E-W) acceleration waveforms from the 25 September 2014 (M 6.2) earthquake at epicenter distance of 102.1 km. Propagating waves from basement to roof shows an amplification in the order of 3.4. The floor numbers and their corresponding height relative to the ground (first floor) are depicted; dot indicates the maximum roof acceleration in the order of 147.1 cm/s^2 .

(2009) and Rahmani *et al.* (2015a) suggest that the response also depends on the rocking at the foundation level when one considers models with soil-structure interaction, such as horizontal and rocking motions, for which the

response is coupled. In such cases, the dispersive wave propagation may occur, and the pure shear-beam model assumption may not be valid (Ebrahimian and Todorovska, 2015).

Cross Correlation

It has been demonstrated theoretically and experimentally that the cross correlation of recordings at two receivers can be used to estimate the Green's function of a wave between the receivers (Snieder, 2004, 2007; Sabra *et al.*, 2005; Wapenaar *et al.*, 2011). The cross correlation of $u(z, \omega)$ and $u(z_a, \omega)$ is

$$C(z, z_a, \omega) = u(z, \omega)u^*(z_a, \omega) = |S(\omega)|^2 \frac{\{e^{ikz}e^{-\xi|k|z} + e^{ik(2H-z)}e^{-\xi|k|(2H-z)}\}\{e^{-ikz_a}e^{-\xi|k|z_a} + e^{-ik(2H-z_a)}e^{-\xi|k|(2H-z_a)}\}}{1 - R(\omega)e^{2ikH}e^{-2\xi|k|H} - R^*(\omega)e^{-2ikH}e^{-2\xi|k|H} + |R(\omega)|^2e^{-4\xi|k|H}}, \quad (7)$$

in which $u(z, \omega)$ is the response at the height z , and $u(z_a, \omega)$ is the response at the reference height z_a . The incoming wave $S(\omega)$ and reflection coefficient $R(\omega)$ indicate that the results of the cross correlation depend on the foundation coupling. This makes estimation of the building properties, such as shear-wave velocity and intrinsic attenuation, more intricate than that from deconvolution because the former does not separate the soil-structure interaction effects.

Results

Both deconvolution and cross correlation were applied to the horizontal components of waveforms recorded in the building from five earthquakes, listed in Table 2, and ambient-vibration data. The structural responses $u(z, \omega)$ from instrumented floors were first deconvolved by the structural response measured at the roof $u(H, \omega)$ for two orthogonal directions separately. Full lengths of the waveforms were used because the building's response remained essentially elastic (this will be discussed later). The deconvolved waveforms (i.e., IRFs) were band-pass filtered with corner frequencies of 0.2 and 8 Hz using a second-order acausal (zero phase-shift) Butterworth filter to accentuate at least three fundamental modes using recorded motions in E-W, N-S, and floor rotational motions. Taking the difference in horizontal motions from two parallel accelerometers located on the same floor and then normalizing this difference with the distance between the two sensors with an assumption that floor diaphragms remained rigid implied the floor rotational motions.

The same Butterworth filter with corner frequencies of 0.2 and 8 Hz is also used for the CFs. The IRFs and CFs have a sampling rate of 200 samples per second, matching the recorded data. Figure 8 illustrates the IRFs computed for the E-W direction using the waveforms shown in Figure 7. The IRFs without reflections and late arrivals suggest that the wave propagation is essentially 1D for the frequency envelope chosen. The IRFs contain energy in the acausal part because there is no physical source at the roof. If the waveforms are deconvolved with the waveform at the basement, they will not display acausal arrivals, and resultant IRFs will be more complicated due to late arrivals and reflected waves.

In such cases, it will be difficult to pick the arrival times precisely. The causality properties of the deconvolved waveforms are therefore related to the existence (or nonexistence) of a physical source of the recorded waves (Snieder *et al.*, 2006).

The IRF at the roof is a band-pass-filtered Dirac delta function (virtual source) because any record deconvolved with itself, with white noise added, yields a Dirac delta func-

tion (pulse) at $t = 0$ (see equation 2 with $z = z_a = H$), as can be seen in Figure 8. The deconvolved waveforms across all floors demonstrate a wave state of the structure. This wave state is the response of different parts of the structure to the Dirac delta function at the roof. For early times, the pulse travels downward, and the response is the superposition of one upward and one downward traveling wave. The absence of waves reflected off the floors may be due to the relatively low frequencies in the waveforms used in this study. At $t = 0$, the wavefield is nonzero at the top three floors, due to the limitation of the spatial resolution. For later times, however, the waveforms are governed by structure resonance that decays exponentially with time due to attenuation (intrinsic damping). For example, in Figure 8, the amplitudes of the downward traveling waves (in the positive times) are generally smaller than the corresponding amplitudes of the upward traveling waves (in the negative times) as a result of the damping in the structure.

Figure 9 shows the cross correlation of the acceleration waveforms shown in Figure 7 with the waveform at the first floor. The wave propagation between the receiver at the first floor and the receiver at other floors are reconstructed. The time lags in propagating waves in the structure (from the first floor to the roof) can be clearly seen from the peaks (marked by dots) of CFs. The wave propagation at the top two stories is complicated because of the wave reflection from the roof, which also indicates that the results of cross correlation are dependent on the reflection coefficient $R(\omega)$. The wave propagation can also be observed in the acausal part, which is different from the results of deconvolution, when the base is used as a virtual source (Fig. 9). This phenomenon is consistent with the results of Nakata *et al.* (2013).

Shear-Wave Velocity

The shear-wave velocity of traveling waves ($V_{S,n}$) for the n th layer between two receivers can be derived based on the time lag τ between peaks of IRFs and CFs and the travel distance following the ray theory, which disregards wave scattering (i.e., $V_{S,n} = h/\tau$, in which h is the distance in meters). As shown in Figure 10, we modeled the building as a simple three-layer elastic shear beam according to the

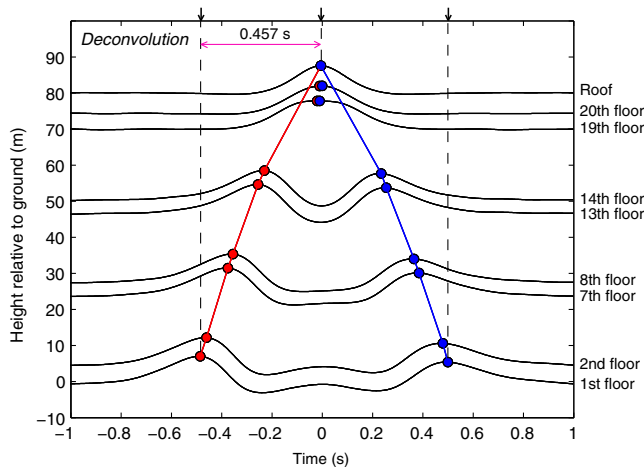


Figure 8. Deconvolved waveforms, calculated from the 25 September 2014 (M 6.2) earthquake E-W direction acceleration time series, are plotted as positive and negative amplitudes for each instrumented floor over time. Virtual source is at the roof, thus the deconvolved waveforms are acausal. Frequency range of the waveforms is 0.2–8 Hz. The color version of this figure is available only in the electronic edition.

receiver locations. The layers, consisting of groups of floors, are assumed to be homogenous isotropic perfectly bonded to each other. This model, appropriate for moment-frame structures over certain frequency bands (Rahmani and Todorovska, 2013), is supported by a half-space and excited by vertically incident plane shear waves without foundation rocking. The rocking motion at the basement level of the building was computed by taking the difference in vertical motions recorded by sensor numbers 3, 4, and 6 in Figure 4. The maximum transient tilt among all events, determined as 1.5×10^{-5} radian for the 2014 earthquake, does not reveal any foundation rocking.

For deconvolution, the shear-wave velocities computed from the velocity of upward and downward traveling waves are averaged. Figure 11 shows the shear-wave velocity profiles based on the two methods for the E-W, N-S, and floor rotational motions considering five earthquakes for the 0.2–8 Hz frequency range. The shear-wave velocities along the building height gradually decrease from the top to the base according to the shape of the fundamental mode (as can also be clearly seen in Fig. 7). The mode shape is related to distribution of mass and stiffness in the building and boundary conditions. The stiffness is specified by strength (modulus of elasticity), geometry, and section size of structural elements. Therefore, the reduction in shear-wave velocity at the upper floors is attributed to the less stiff upper portion of the building than the lower portion because the section size of structural components reduces toward the upper floors.

In the case of deconvolution, the variation of shear-wave velocity is more pronounced for the floor rotational response. For cross correlation, the interevent variation of shear-wave velocity is higher than the deconvolution, because the results

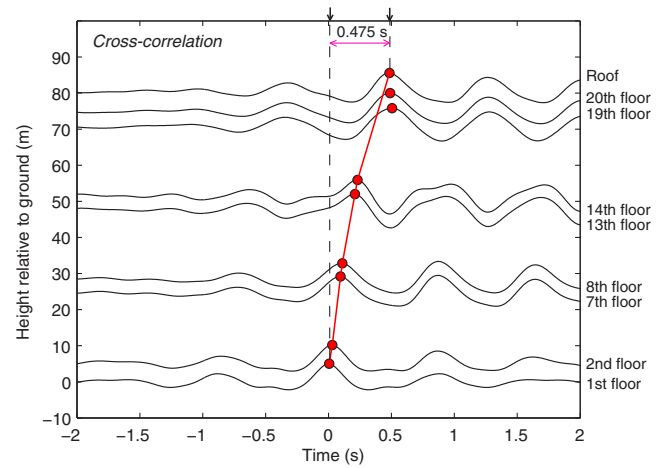


Figure 9. Cross correlation of waveforms, calculated from the 25 September 2014 (M 6.2) earthquake E-W direction acceleration time series, are plotted as positive and negative amplitudes for each instrumented floor over time. Vertical arrows are used to estimate one-way travel times (upward traveling waves). Frequency range of the waveforms is 0.2–8 Hz. The color version of this figure is available only in the electronic edition.

of cross correlation are dependent on incoming wave $S(\omega)$ and reflection coefficient $R(\omega)$, though the general trend of shear-wave velocity along the building height is similar to that of the deconvolution results. The median and standard deviation of height-wise shear-wave velocity distributions determined using the deconvolution and cross correlation from five earthquakes considering the E-W, N-S, and floor rotational motions are compared in Figure 12. The shear-wave velocity from the deconvolution demonstrates lower variability than those from the cross correlation. The deconvolution and cross correlation produce similar results, around 150 m/s, at the top part of the building (layer 1). However, the difference between the two methods becomes pronounced for other layers. The shear-wave velocities for the torsional response are generally smaller than those of the E-W and N-S responses.

We also determined the median shear-wave velocity of the entire building using the three-layer shear-beam model by considering sampling rate uncertainty. An example is shown in Figure 13a, in which the square and circular marks correspond to the time of the peaks in the IRFs similar to those portrayed in Figures 8 and 9. In these figures, the vertical bars at each observation point indicate a ± 0.005 s sampling interval. The travel distance, assumed to be exact, is measured relative to the position of the virtual source (i.e., the roof for the deconvolution and the first floor for the cross correlation). The negative travel distance is for the upward traveling wave. A straight line was fitted to the distance and time pairs identified from the upward and downward traveling waves using least squares. This process was repeated by randomly adding time uncertainty to time pairs via Monte Carlo simulation. A total of 1000 simulations were conducted. The time uncertainty was assumed to have a uniform

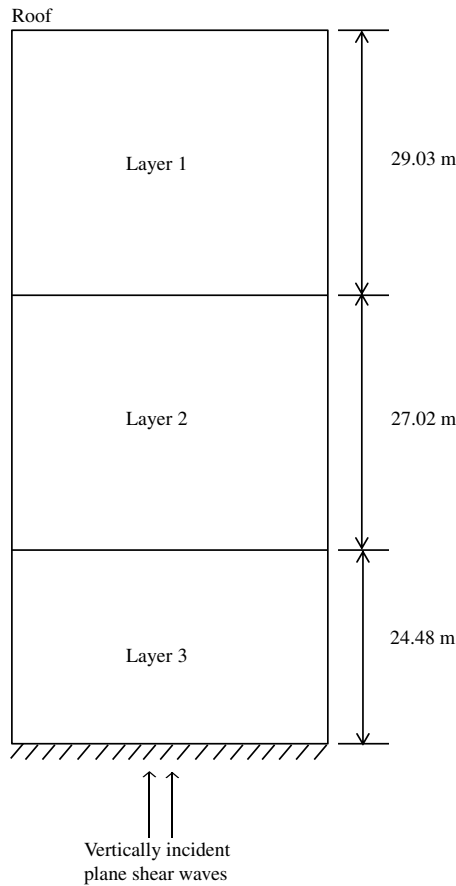


Figure 10. Correspondence between layers and floor numbers for the three-layer shear-beam model used to calculate the average shear-wave velocity of the Atwood Building; heights of layers are depicted.

distribution between -0.005 and 0.005 s. This way, measurement errors were propagated to the shear-wave velocities estimated.

The same method was also applied to the results of cross correlation; however, no negative distance appears in Figure 13b, because only the upgoing waves are identified. The shear-wave velocities of the entire building, computed considering five earthquakes, are listed in Table 3. The time-sampling uncertainty on the resultant shear-wave velocities is less than 1%. The median shear-wave velocities along the E-W direction is in general 10% less than those along the N-S direction because the averaged stiffness of the building along the N-S direction is slightly larger than that along the E-W direction—this is evident from the greater openings in the concrete core along the E-W direction than those along the N-S direction, as shown in Figure 3b. The variation of shear-wave velocity can be observed for different earthquakes. The results of the first four earthquakes (events 1–4) are relatively stable, whereas the result of the fifth earthquake (event 5) shows a reduction. This is attributed to a lesser contribution of nonstructural components, attached permanently to the structure, to overall stiffness of the building under this event, which has greater recorded

amplitudes in the building than those from the other four earthquakes. This part will be explained later in the [Contribution of Nonstructural Components to Building's Lateral Stiffness](#) section.

Predominant Frequencies and Mode Shapes

For a homogenous isotropic shear beam with 1D wave-propagation model, the predominant frequency (f) can be derived from the shear-wave velocity (V_s) as $f = V_s/4H$, in which H is the total height. The predominant frequency derived by this simple formula is presented in Table 4 using the recorded motions in the E-W and N-S directions, as well as using the floor rotational motions. For comparison, the predominant frequency of the structure is also computed from the complex mode indicator function (CMIF), which is based on the singular value decomposition of multiple reference frequency response functions (FRFs; [Shih et al., 1988](#)). The FRF is computed as

$$H(f) = P_{xx}(f)/P_{xy}(f), \quad (8)$$

in which P_{xx} is the power spectral density of the structural response measured at the roof, and P_{xy} is the cross power spectral density of the structural response measured at the roof and at the first floor. Equation (8) is inverted compared with most uses of this method ([Rades, 2010](#)). A detailed review of the CMIF can be found in [Allemang and Brown \(2006\)](#).

The number of CMIF curves is equal to the number of recording locations. Figure 14 presents a typical CMIF curve for multiple reference sets of input data. The largest singular values have peaks at the damped natural frequencies. Therefore, one can easily detect the first three predominant frequencies from the CMIF for the E-W, N-S, and rotational responses. Those identified frequencies are listed together with the derived frequencies from the shear-wave velocity in Table 4. We extracted the first three fundamental modes of the building independently using the recorded motions in the E-W and N-S directions, as well as using the floor rotational motions. Although the first two modes correspond to bending shear, the third mode is torsion. For the five earthquakes, the relative difference between the largest and lowest predominant frequencies is 14% for the translational and 24% for the torsional response. The relative differences between the largest and lowest second- and the third-mode frequencies are within 10% of the translational directions and up to 28% of the torsion. The frequencies identified from the 25 September 2014 (M 6.2) earthquake data are generally lower than those identified from other events, and this phenomenon is consistent with the shear-wave velocity results in Table 3.

The average values of the fundamental frequency (first mode) from five earthquakes are 0.46, 0.53, and 0.51 Hz, respectively, for the E-W, N-S, and rotational responses. These results are close to 0.47 and 0.58 Hz, reported in

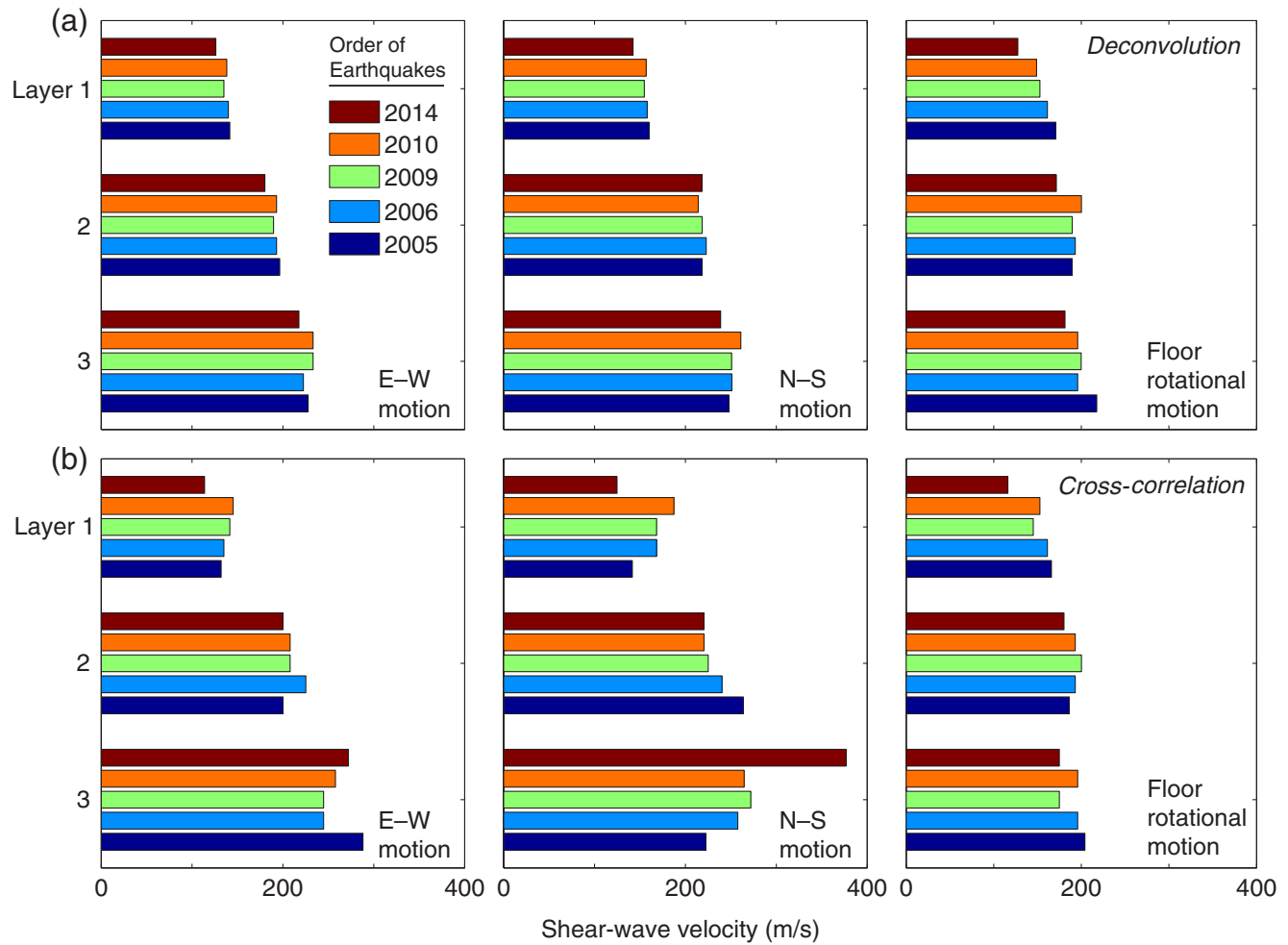


Figure 11. Shear-wave velocity profiles of the Atwood Building for E-W, north-south (N-S), and torsional responses considering a three-layer shear-beam model and five earthquakes. Results are based on (a) deconvolution and (b) cross correlation for the frequency range of 0.2–8 Hz (layer 1, upper floors; layer 3, lower floors; earthquakes are in descending order at each layer). The color version of this figure is available only in the electronic edition.

Çelebi (2006) based on a single distant event (6 April 2005 M 4.9 earthquake with epicenter distance of 183 km). This is also one of the events used in our study. The predominant frequencies are primarily for the fix-based structure because no rocking took place at the foundation level during any earthquakes. For the five earthquakes, the predominant frequency derived from the median shear-wave velocity of the structure is 15% greater than that computed from the CMIF; this difference is due to the crudeness of the estimated fundamental frequency from the shear-wave velocity by the simple formula, which does not consider any bending deformation (Ebrahimian and Todorovska, 2014) and assumes that the building's response is pure shear. The average ratios of the second- and third-mode frequencies to the first-mode frequency are close to the characteristics of the analytical shear beam, having the frequency ratio of 1:3:5. For example, the ratios are 1:3.34:5.52 for the E-W response, 1:3.43:5.56 for the N-S response, and 1:3.22:5.95 for the rotational response for the 2014 event. If these ratios alter significantly from the

analytical ratios, there would be a need to include bending deformations in addition to shear deformations (Boutin *et al.*, 2005; Ebrahimian and Todorovska, 2015).

We found that the vertically propagating shear waves may include small dispersion. It means that the variation of phase velocity within the frequency band analyzed (0.2–8 Hz) is not large. This is apparent from the ration of f_2/f_1 , which is 3.34 for E-W, 3.43 for N-S, and 3.22 for torsion, being greater than 3 (the theoretical value for shear beam). This small dispersion cannot be attributed to the foundation rocking because it did not take place during any of the earthquakes. The building is not a pure moment-frame structure (Fig. 3); it has a concrete core, which is stiff in shear, and therefore deforms in bending in addition to shear, which is likely the main cause of small dispersion within the frequency band analyzed.

The first six mode shapes and their frequencies are illustrated in Figure 15 using the waveform data of the 25 September 2014 M 6.2 earthquake. The mode shapes correspond-

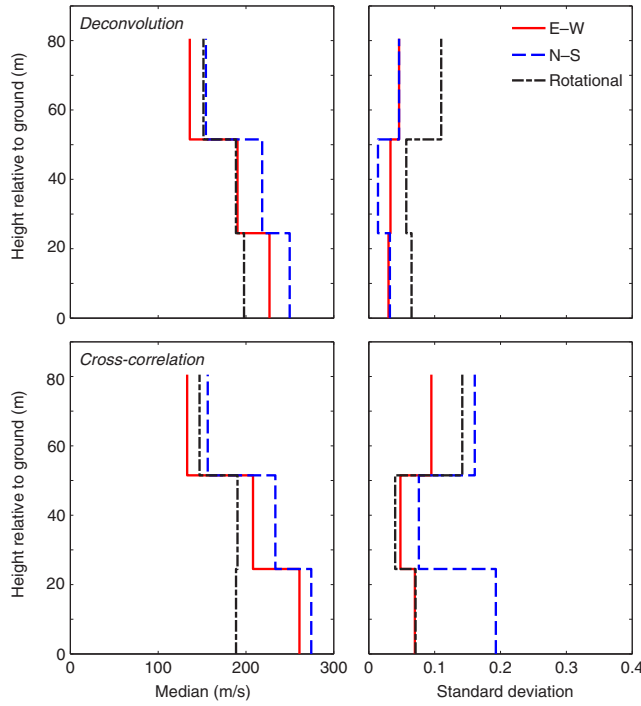


Figure 12. Median and variability of shear-wave velocity based on the three-layer shear-beam model considering five earthquakes. The color version of this figure is available only in the electronic edition.

ing to 0.41 and 0.48 Hz are the first bending-shear modes in the E-W and N-S directions, respectively. The modes with 1.37 and 1.65 Hz are the second bending-shear modes in E-W and N-S directions, respectively. The modes with 2.65 and 2.67 Hz are essentially the same torsional mode obtained separately by analyzing the E-W and N-S directions' motions recorded separately. The first bending-shear modes (in the E-W or N-S directions) are very close to the analytical solution of the shear beam, and no clear coupling can be found between two translational directions (the curve with diamond marks in E-W and the curve with circle marks in N-S directions are close to the vertical zero reference line). It means that the first- and second-mode shapes along the E-W and N-S directions are well separated from each other—an attribute of the symmetric plan building.

The ambient data recorded on 13 December 2003 with a length of 1014 s is also used to identify the frequencies of the structure using the CMIF, in which the FRF is replaced by the cross power spectral density function based on the assumption that the ambient excitation is taken as a white noise. For the civil engineering applications, this assumption can lead to the reasonable estimations of vibration modes. The frequencies identified from the ambient data are generally larger than those identified from the earthquake data. The difference between results of ambient data and results of earthquake data is 17% for translational predominant frequencies and 28% for torsional predominant frequencies. For second- and third-mode frequencies, this difference is generally within 10% for the translational directions.

Contribution of Nonstructural Components to Building's Lateral Stiffness

Buildings almost always work as integrated systems, which include both structural and nonstructural components. Thus, nonstructural components may make notable contributions to the building's overall lateral stiffness. However, this contribution often reduces as the excitation intensity increases because the gaps between nonstructural and structural components open up. If there is no postevent damage in the building, the gaps close gradually, and nonstructural components' contribution to the building's lateral stiffness often recovers to its pre-event condition. This is one of the reasons that the ambient vibration measurements yield building frequencies higher than those computed from measurements during nondamaging earthquakes.

To assess whether there is any nonlinearity in the response of the building even at small strains, we plot the roof drift ratio (the relative maximum drift between the roof and the base normalized by the building height) from five events against the building's first-mode frequencies and median shear-wave velocities using the three-layer shear-beam model along the N-S and E-W directions considering the five earthquakes in Figure 16. This figure clearly shows the trend that because the roof drift ratio increases, the first-mode frequency and wave velocity drop. The first-mode frequencies and wave velocities are consistent among the four earthquakes between 2005 and 2010, which resulted in similar roof drift ratios. The notable reductions in first-mode frequency and wave velocity, which are same in the N-S and E-W directions, occur for the 2014 event.

The modal frequency is a single global parameter that depends on the mass, the stiffness distribution in the structure, and boundary conditions. It is shown by Roux *et al.* (2014) using a beam model that the detection and localization of local perturbations are possible by analysis of changes in modal frequencies. In lieu of time-domain tracking of changes in modal frequencies, we focused on the mode shapes, which represent the deflection patterns of the structure at resonance frequencies, and each component of the mode shape vector carries information corresponding to the location where a motion sensor is placed in the building. Figure 17a shows the first three mode shapes after each earthquake excitation. To measure the correlation between two sets of mode shape vectors, the modal assurance criterion (MAC) is used. The MAC is devised to provide a single numerical value that indicates the correlation between mode shapes (Allemang and Brown, 1982; Allemang, 2003; Pastor *et al.*, 2012). When two mode shapes are fully correlated, the corresponding MAC has a value of 1, whereas fully uncorrelated mode shapes are indicated by a MAC value of 0. The formulation of MAC is

$$\text{MAC}_{mnr} = \frac{|\sum_{q=1}^{N_0} \phi_{mqr} \phi_{nqr}^T|^2}{\sum_{q=1}^{N_0} \phi_{mqr} \phi_{mqr}^T \sum_{q=1}^{N_0} \phi_{nqr} \phi_{nqr}^T}, \quad (9)$$

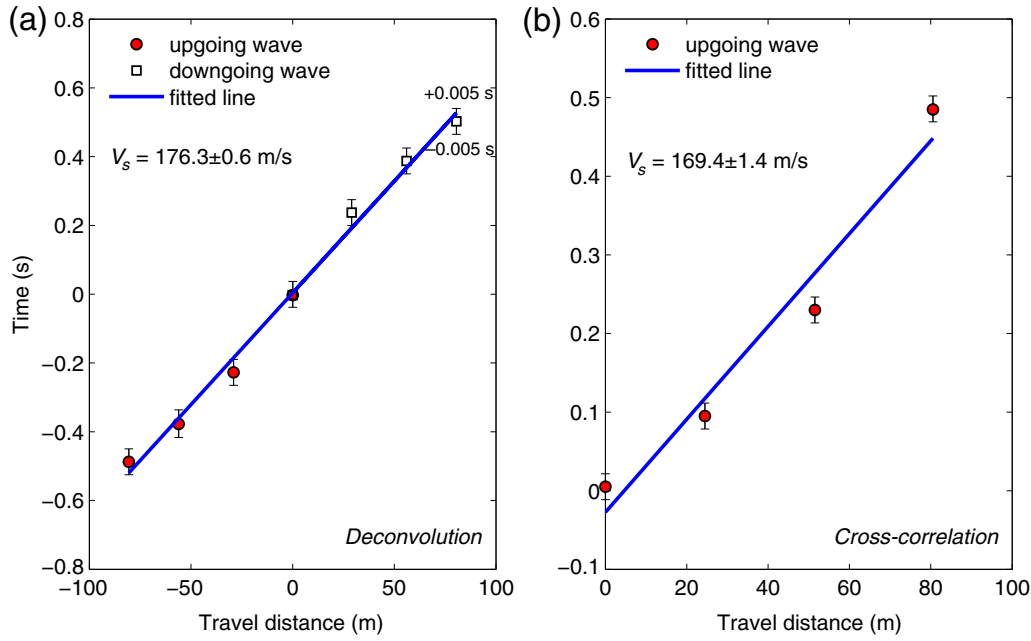


Figure 13. Shear-wave velocity of the building calculated based on the three-layer shear-beam model using the time of the peaks in (a) impulse response functions (IRFs); a negative travel distance/time corresponds to the upward traveling wave and a positive travel distance/time refers to the downward traveling wave; (b) correlation function (CF); no negative distance appears because the upward traveling wave is identified only from the CFs. In (a) and (b), a straight line is fitted to all data points by least squares to determine the average shear-wave velocity in the building. The least-squares solutions to the slope are 176.3 ± 0.6 and 169.4 ± 1.4 (\pm indicates measurement error due to sampling rate uncertainty determined by Monte Carlo simulations), respectively, for the deconvolution and cross correlation. Data correspond to the E-W direction waveforms of the 25 September 2014 (M 6.2) earthquake. The color version of this figure is available only in the electronic edition.

in which ϕ_{mqr} is the modal coefficient for the degree-of-freedom q , mode r , and N_0 is the number of degrees of freedom. The subscript m indicates the first excitation, and the subscript n denotes the second excitation. Superscript T is the transpose operator. Using equation (9), the mode shapes after each earthquake following the 2005 event are compared with those of the 2005 event. The resultant MAC values, listed in Table 5, show that the changes in the mode shapes between earthquakes are insignificant as compared with the changes in the frequencies.

The localized damage in the structure may also be identified with the help of curvature mode shape because it is

directly related to the flexural stiffness of elements' cross sections (Pandey *et al.*, 1991). We computed the curvature mode shapes by fitting polygons to the mode shapes and then calculating the analytical curvatures from the polygons. We identified no changes in the curvature mode shapes for the first two modes, and changes are marginal for the third mode (Fig. 17b). Thus, we attribute variations in frequencies (and shear waves) that we observed during the stronger 2014 event to the opening and closing of gaps between the non-structural and structural components. Although the nonlinear response of soil even for weak motion could affect such variations, the site response of the Atwood Building was found

Table 3
Shear-Wave Velocity of the Atwood Building Based on Deconvolution and Cross Correlation

Direction	Event					Median	Ambient
	1	2	3	4	5		
Deconvolution							
East-west	198.1 ± 0.8	197.8 ± 0.8	190.7 ± 0.7	192.6 ± 0.7	176.3 ± 0.6	191 ± 0.7	193 ± 0.8
North-south	207.4 ± 0.8	210.3 ± 0.9	206.4 ± 0.8	209 ± 0.9	193.2 ± 0.7	205.2 ± 0.8	216 ± 0.7
Rotational	182.7 ± 0.6	183.2 ± 0.6	176.7 ± 0.6	181.8 ± 0.6	158.2 ± 0.5	176.3 ± 0.6	210 ± 0.6
Cross Correlation							
East-west	183.4 ± 1.6	187.5 ± 1.7	186.3 ± 1.7	190.3 ± 1.7	169.4 ± 1.4	183.2 ± 1.6	208 ± 1.5
North-south	197.4 ± 1.8	213.7 ± 2.2	211.3 ± 2.0	217.4 ± 2.3	192.6 ± 1.8	206.2 ± 2.0	227 ± 1.9
Rotational	183 ± 1.6	181.9 ± 1.6	171.8 ± 1.4	178.1 ± 1.5	151.3 ± 1.1	172.8 ± 1.4	232 ± 1.6

Unit is in meters per second. Plus/minus symbol indicates measurement error due to sampling rate uncertainty determined by Monte Carlo simulations.

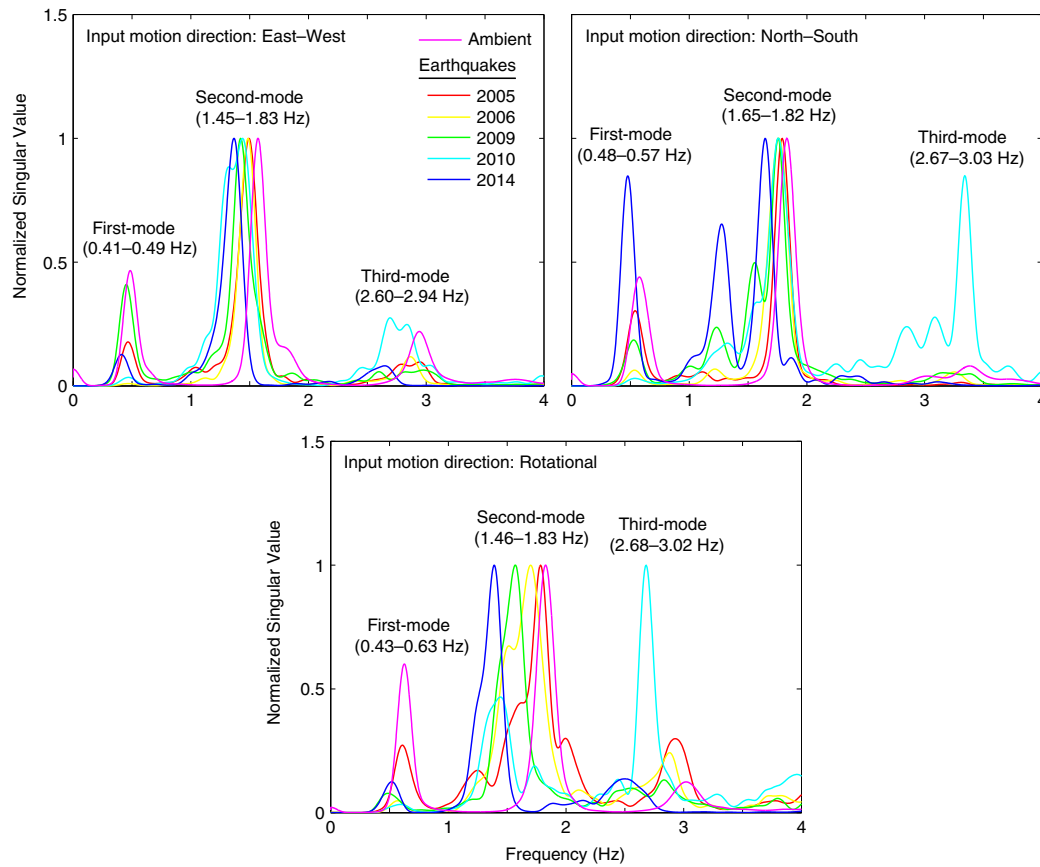


Figure 14. First three fundamental-mode frequencies identified in E-W, N-S, and torsional responses by complex mode indicator function (CMIF) using the waveform data from five earthquakes (listed in Table 1) and ambient vibrations. The color version of this figure is available only in the electronic edition.

to be elastic during these earthquakes based on analyses of waveforms from the nearby geotechnical array in Delaney Park (E. Kalkan et al., unpublished manuscript, 2017; see [Data and Resources](#)).

Intrinsic Attenuation

During wave propagation, the energy loss induced by intrinsic damping can be represented by the following attenuation equation:

Table 4

Building Vibration Frequencies Identified by the Wave Propagation Method [$V_s/(4H)$] and the Complex Mode Indicator Function for Mode 1, 2, and 3 Using Recorded Horizontal Motions in the Building along East–West and North–South Directions as well as Inferred Floor Rotational Motions

Direction of Input Motion	Mode Shape		Event					Ambient
			1	2	3	4	5	
East–west		$V_s/(4H)$	0.61	0.61	0.59	0.60	0.55	0.60
	Bending shear	Mode-1	0.46	0.47	0.45	0.47	0.41	0.49
	Bending shear	Mode-2	1.49	1.49	1.42	1.44	1.37	1.57
	Torsion	Mode-3	2.79	2.86	2.60	2.70	2.65	2.94
North–south		$V_s/(4H)$	0.59	0.59	0.58	0.58	0.55	0.67
	Bending shear	Mode-1	0.54	0.54	0.53	0.54	0.48	0.57
	Bending shear	Mode-2	1.79	1.76	1.75	1.75	1.65	1.82
	Torsion	Mode-3	2.94	2.79	2.70	2.85	2.67	3.03
Rotational		$V_s/(4H)$	0.57	0.55	0.53	0.53	0.46	0.65
	Bending shear	Mode-1	0.54	0.46	0.43	0.52	0.45	0.63
	Bending shear	Mode-2	1.63	1.52	1.55	1.70	1.45	1.83
	Torsion	Mode-3	2.70	2.68	2.62	2.78	2.68	3.02

Unit is in hertz (mode shapes of frequencies italicized are shown in Fig. 15).

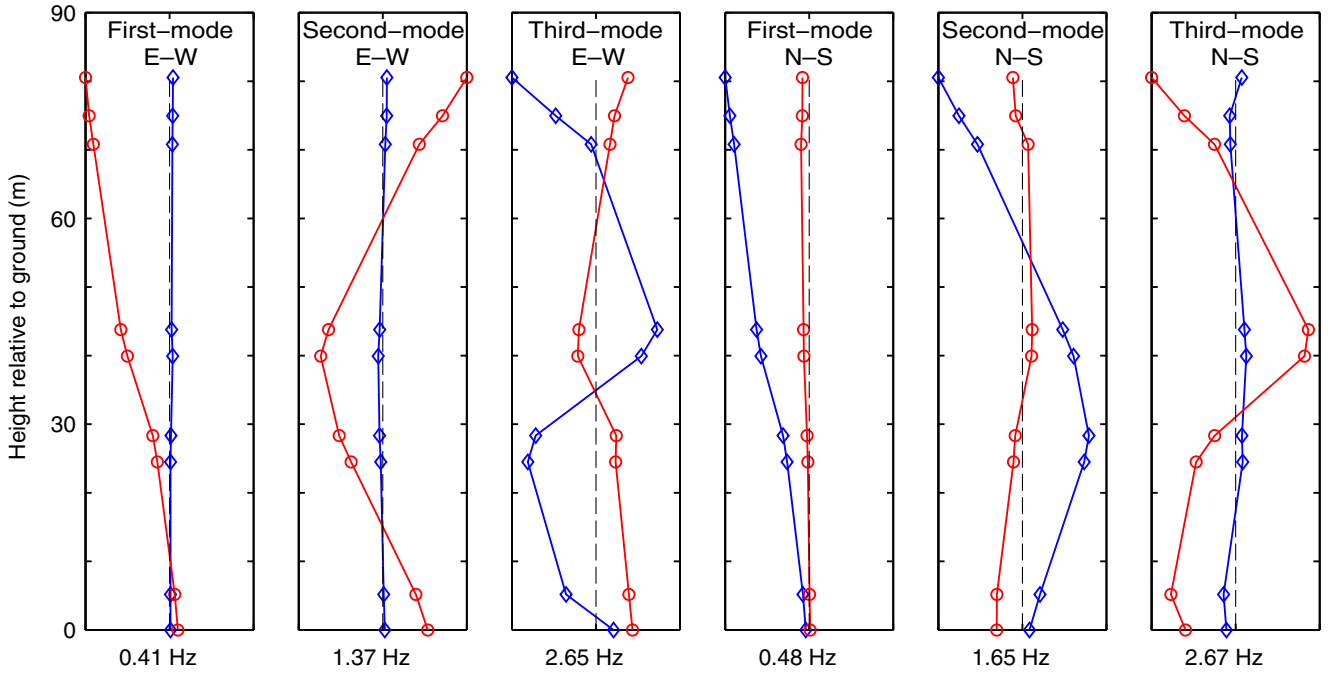


Figure 15. First six fundamental-mode shapes and frequencies identified by CMIF using the waveform data of the 25 September 2014 (M 6.2) earthquake. Modes are well separated from each other with insignificant coupling—apparent from contributions of curves identified by circle and diamond marks. 0.41 and 1.37 Hz are first and second bending-shear modes along E-W direction, and 2.65 Hz indicates torsional mode. Similarly, 0.48 and 1.65 Hz are the first and second bending-shear modes along the N-S direction, and 2.67 Hz denotes torsional mode (curve with diamond marks denotes N-S component of the mode shape, and curve with circle marks denotes E-W component of the mode shape). The color version of this figure is available only in the electronic edition.

$$A_s(f) = \exp\left(-\pi \times f \times \frac{\tau}{Q}\right) \quad (10)$$

(Aki and Richards, 2002), in which $A_s(f)$ is the reduction in the amplitude of a sinusoidal wave frequency f when it travels a distance of travel time τ , and Q is the quality factor. To evaluate the intrinsic attenuation in structures, previous studies (Snieder and Şafak, 2006; Prieto *et al.*, 2010; Newton and Snieder, 2012; Nakata *et al.*, 2013) used equation (10) in conjunction with the IRFs; the same approach is adapted here because it separates the intrinsic attenuation and radiation damping.

First, the recordings at different floors were deconvolved with the recordings at the first floor to generate causal IRFs. The IRFs are filtered around the resonant frequencies using a second-order acausal Butterworth band-pass filter with corner frequencies of 0.2–1.0 Hz for the first mode, 1.0–2.0 Hz for the second mode, and 2.0–3.0 Hz for the third mode, and finally the envelope is plotted. The natural logarithm of the envelopes of the band-pass-filtered waveforms corresponding to the 25 September 2014 (M 6.2) earthquake is shown in Figure 18. To separate the curves at different heights, an offset equal to the floor number is added to the natural logarithm of the envelope. The slope of the curves depends on the wave attenuation, thus the offset has no influence on the results. The slopes of the curves, which are similar at different floors, were computed in the least-squares sense between

t_1 and t_2 . The decay of the natural logarithm of the envelope follows the rule between t_1 and t_2 , defined by equation (10), whereas the exponential decay is not valid for the later times (Snieder and Şafak, 2006). The values of t_1 and t_2 are determined by inspecting the deconvolved waveforms of different earthquakes. The slope of the fitted line is equal to $-\pi f/Q$. Using different instrumented floors, one may obtain uncertainty measurements. The consistency of Q values for each instrumented floor indicates the measurement accuracy. The mean slope at different layers (which is generally consistent at different floors) and the first-mode frequencies identified with the CMIF method (see Table 4) were used to compute the average Q and ξ . Table 6 summarizes the results for all events. The damping in the E-W direction is slightly larger than that in the N-S direction. The variability of the damping ratio is moderate with a coefficient of variation of 16%. The average damping ratio is found to be 3.7% and 3.4% along the E-W and N-S directions, respectively, for the fundamental modes. The E-W-damping value is 8.8% more than the N-S-damping value. These two damping values are close to each other because of square plan and near-symmetrical distribution of load bearing elements. We interpret the damping primarily as that of the structure because of insignificant foundation rocking observed during five earthquakes, which curtails the contribution of radiation damping.

The previous study reported the first-mode modal-damping values as 4.2% and 2.7% along the E-W and N-S directions,

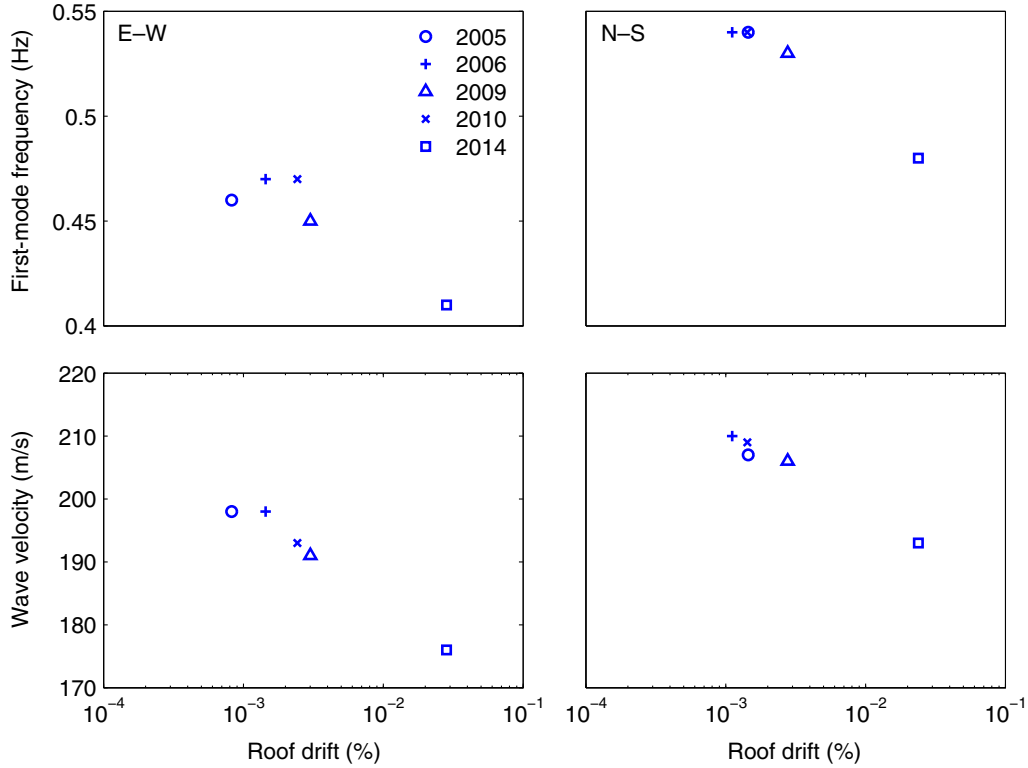


Figure 16. Frequencies of fundamental modes estimated using CMIF, and shear-wave velocities based on three-layer shear-beam model in (a) E-W and (b) N-S directions considering five earthquakes (listed in Table 1). Roof drift ratio (given in percentage) is the maximum absolute roof displacement divided by the building height. X axes are in logarithmic scale. The color version of this figure is available only in the electronic edition.

respectively, using the data from the 6 April 2005 **M** 4.9 earthquake (Celebi, 2006). The E-W-damping value is 55% more than the N-S-damping value. For this event, we computed the first-mode modal-damping values as 3.7% and 3.1% along the E-W and N-S directions, respectively. The ambient-vibration data (stacked at every 60 s) are also used to identify the intrinsic damping. Those results are not shown here because of their large variation, and they are not as consistent as those obtained from the earthquake data.

Prediction of Building's Elastic Response Using IRFs

The IRFs computed from an earthquake can serve as a proxy to predict the building's response to another earthquake provided that the input motion is available from the second earthquake for convolution, and the building response remains in elastic regime during both events (Prieto *et al.*, 2010). To demonstrate that the building's elastic response can be predicted reasonably for a given earthquake scenario, we compare floor displacements derived using the trapezoidal integration rule from the observed floor accelerations of the 2014 **M** 6.2 earthquake with the predictions obtained by convolution of the waveforms from the first floor with the previously computed IRFs from the 2005 **M** 4.9, 2006 **M** 4.7, 2009 **M** 5.4, and 2010 **M** 4.9 earthquakes. Figure 19 compares the observations of the displacement re-

sponse of the building with those from the predictions. The predicted displacements are in general similar to the observed ones. The misfit between the predictions and observations is computed as normalized root mean square deviation (RMSD) in the following equations:

$$\text{RMSD} = \sqrt{\left(\sum_{i=1}^n [\hat{u}(t) - u(t)]^2 \right) / n}, \quad (11)$$

in which \hat{u} is the predicted value of observed displacement u and n is the number of data points within the waveform. The normalized RMSD is computed as

$$n\text{RMSD} = \frac{\text{RMSD}}{u_{\max} - u_{\min}}, \quad (12)$$

in which u_{\max} and u_{\min} are the maximum and minimum value of the observed absolute displacements. For plots shown in Figure 19, the $n\text{RMSD}$ ranges between 14.7% and 17.9%. These results indicate that the building response in elastic regime can be effectively predicted using the IRFs.

Predictions of structural motion calculated from IRFs convolved with previously observed weak-to-moderate ground-motion time histories could lead to predictions of the onset of nonlinear response. For instance, if the predicted building response from IRFs of weak motion data does not match with

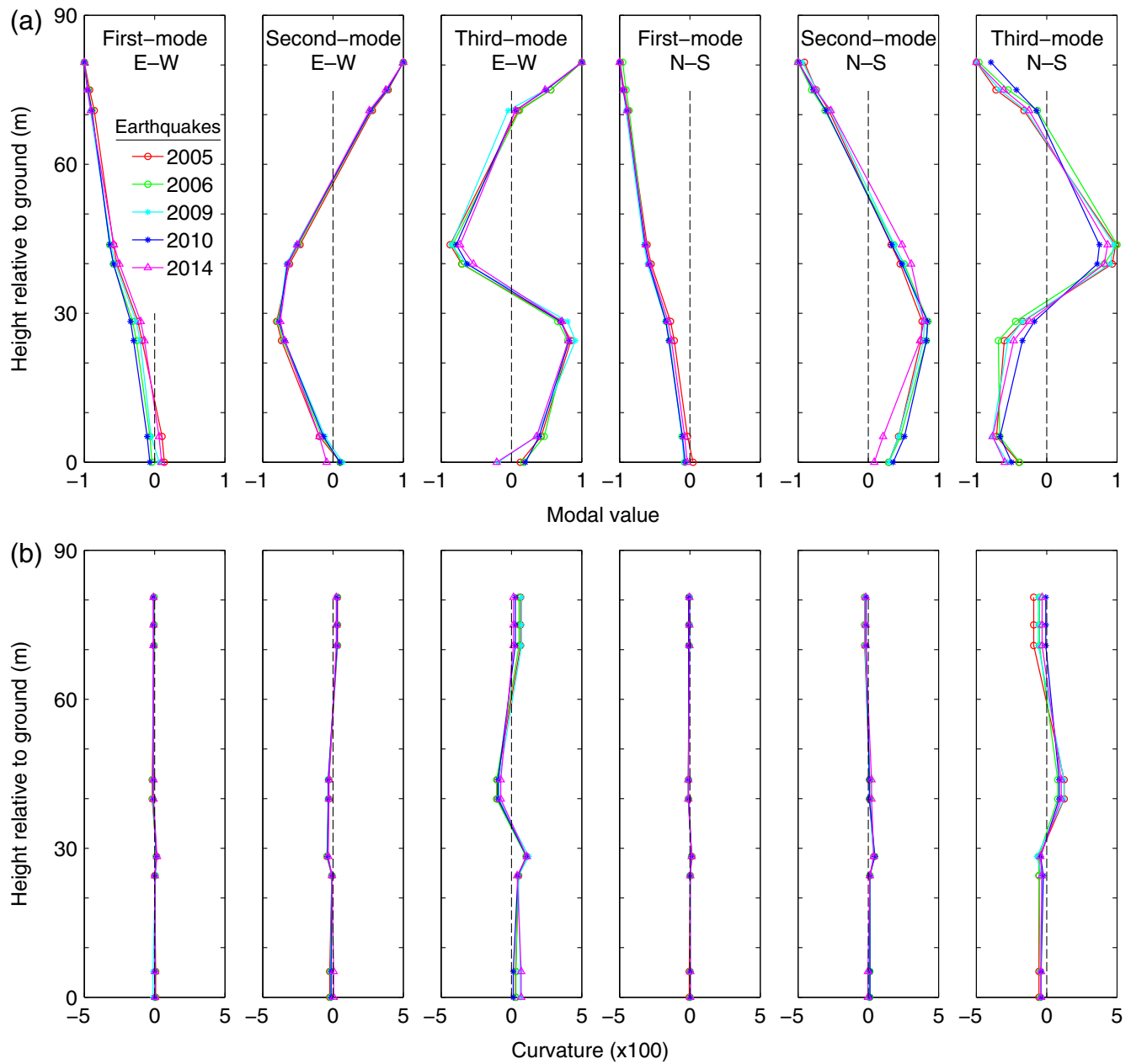


Figure 17. (a) Normalized mode shapes and (b) mode shape curvatures for first three fundamental modes in E-W and N-S directions computed using recordings in the building from five different earthquakes (listed in Table 2). The color version of this figure is available only in the electronic edition.

Table 5

Modal Assurance Criterion (MAC) Values Computed from Two Sets of Mode Shape Vectors after 6 April 2005 **M** 4.9 Earthquake (Event 1) and after Each Following Event

Event	East-West			North-South		
	Mode 1	Mode 2	Mode 3	Mode 1	Mode 2	Mode 3
2	0.979	0.999	0.998	0.991	1.000	0.979
3	0.991	0.996	0.963	0.991	0.999	0.992
4	0.968	0.998	0.995	0.992	0.999	0.964
5	0.997	0.988	0.959	0.997	0.960	0.978

the observations from strong motion after a certain time, the mismatch may be attributed to the onset of nonlinear action in the building.

Conclusions

Deconvolution and cross correlation are applied to the waveform data recorded in a 20-story structure in Anchorage, Alaska, to retrieve vertically propagating shear waves in the building. This structure is an excellent example of a midrise symmetric-plan steel, moment-resisting frame office building, typical of urban settings. The waveform data

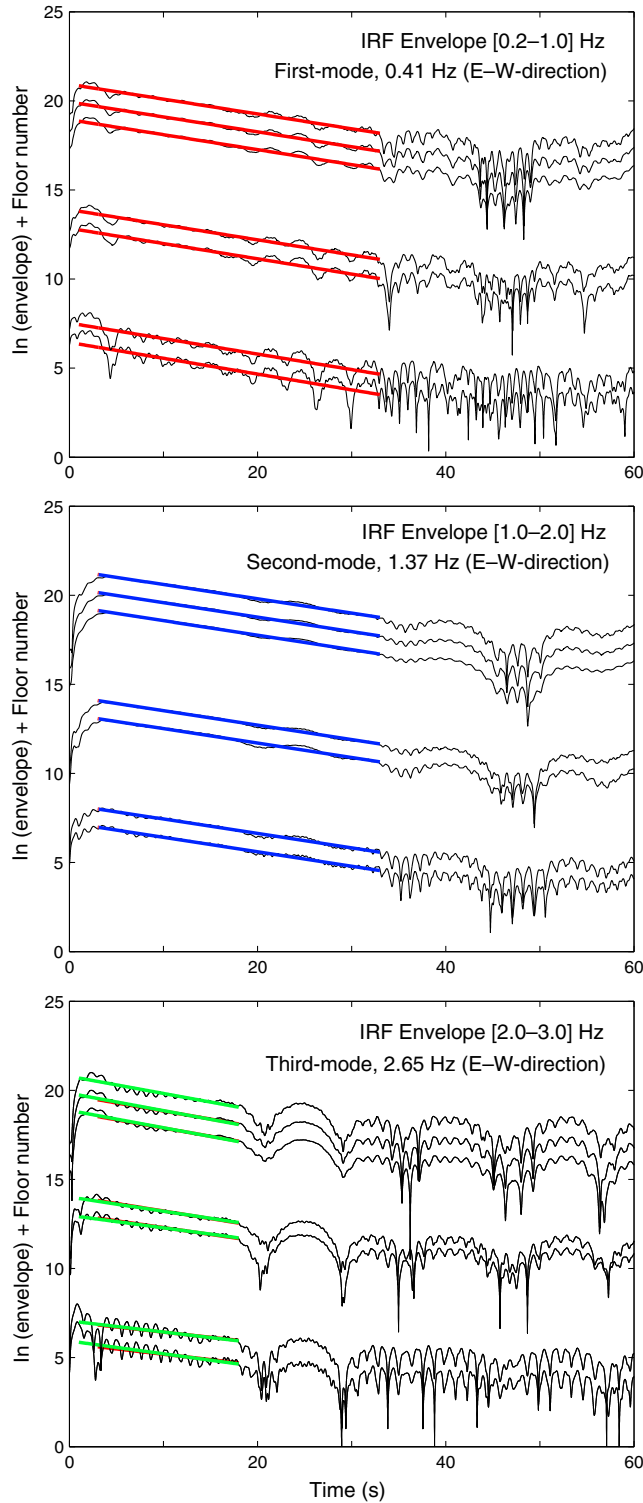


Figure 18. Envelopes of IRFs in natural logarithmic scale for the first three fundamental modes in E-W direction. The data correspond to the 25 September 2014 (M 6.2) earthquake E-W direction. For the first and second modes, curves between 3 and 33 s, and for the third-mode curves between 1 and 18 s are fitted with a straight line using least squares to find the slope. The measured slope yields a quality factor ($Q = -\pi f / \text{slope}$, f = predominant frequency) of 15.1 ± 0.33 for the first mode, 52.9 ± 0.26 for the second mode, and 101 ± 19.33 for the third mode. The variation in estimated Q is much higher for the third mode. The color version of this figure is available only in the electronic edition.

from a 32-channel accelerometer array include accelerations observed from five small and moderate, local and regional earthquakes, and from ambient vibrations. The data are used to compute the IRFs and CFs, which led to estimation of velocities of traveling waves and intrinsic attenuation. The building's fundamental frequencies and mode shapes are obtained using a CMIF based on singular value decomposition of multiple reference frequency-response functions. This work presents a backbone data of system-identification measurements for the undamaged condition of this building, which may be used for tracking changes in structural integrity during and after future earthquakes. The key findings of this study are as follows.

1. The IRFs obtained by deconvolving the recorded motions at different floors of the building with the roof motion are in general similar in two orthogonal horizontal directions. We found that the median shear-wave velocities along the E-W direction are in general 10% less than those along the N-S direction because the averaged stiffness of the building along the N-S direction is slightly larger than that along the E-W direction.
2. The simplicity and resemblance of the IRFs from different earthquakes and ambient-vibration data suggest that a 1D shear beam is generally a reasonable model to quantify the Atwood Building's elastic dynamic properties. This is supported by the fact that the ratio of frequencies identified by the CMIF method is close to those of the analytical shear beam, having the frequency ratio of 1:3:5. For example, the ratios are 1:3.34:5.52 for the E-W response, 1:3.43:5.56 for the N-S response, and 1:3.22:5.95 for the rotational response for the 2014 event. The small differences in the analytical ratios within the frequency band analyzed are attributed to the concrete core of the building, which is stiff in shear, and therefore deforms in bending in addition to shear.
3. The rocking motions of the building during the five earthquakes were found to be insignificant—the maximum transient tilt among all events was computed as 1.5×10^{-5} radian. If it existed, rocking would not only affect the damping due to the soil-structure interaction but would also result in the dispersive response of deconvolved wavefields in the building due to coupling of horizontal and rocking motions.
4. The estimated median shear-wave velocity from IRFs of five earthquakes is 191 m/s for the E-W, 205 m/s for the N-S, and 176 m/s for the torsional responses. The shear-wave velocity is found to be as much as 9% lower for the 2014 event as compared to the median shear-wave velocity from other four events; the 2014 event shook the building more strongly. The MAC and curvature mode shapes demonstrate that the change in the mode shapes is insignificant as compared to the change in the frequencies. The noticeable changes in the mode shapes would be influenced by localized damage in the structure. Thus, we interpret change in shear waves (and frequencies) that

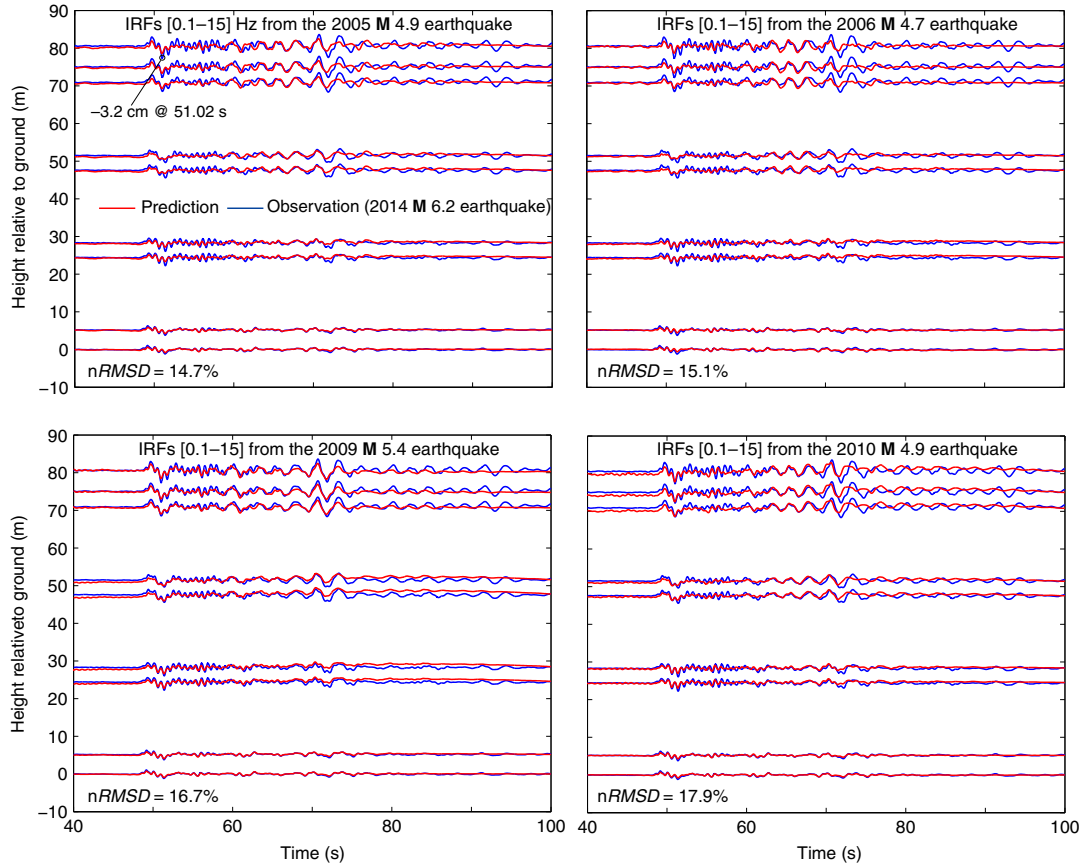


Figure 19. Comparisons of observed floor displacements for instrumented floors derived from the E-W waveforms of the 25 September 2014 (M 6.2) earthquake with those computed by convolving the IRFs of the 6 April 2005 (M 4.9), 27 July 2006 (M 4.7), 22 June 2009 (M 5.4), and 20 September 2010 (M 4.9) earthquakes E-W direction waveforms. The input motion used for predictions is from the M 6.2 earthquake E-W direction waveform recorded at the ground floor. Predicted displacements are similar to the observed displacements; normalized root mean square deviation (*nRMSD*) ranges between 14.7% and 17.9%. Peak value of displacement during the M 6.2 earthquake is 3.2 cm at 51.02 s, occurring at the roof level (same in each panel). The color version of this figure is available only in the electronic edition.

we observe during the stronger event is due to the opening and closing of gaps between nonstructural and structural components.

5. The travel time of waves decreased during the earthquakes as compared to those computed from the ambient vibrations. For example, the median shear-wave velocity values from five events are 1%, 5%, and 16% less than those computed by deconvolution from ambient vibra-

tions. This indicates that nonstructural components are affecting the stiffness of the structure further during ambient measurements. Also, the shear-wave velocities estimated from the earthquake data are more stable than those computed from the ambient-vibration data.

6. According to the properties of deconvolution, the responses are independent from the soil-structure coupling and the effect of wave propagation below the bottom receiver, provided that no foundation rocking takes place. Cross correlation, however, cannot separate the building response from the soil-building coupling and the wave propagation below the virtual source. Because of that, IRFs computed by deconvolution are more stable than those computed by the CFs. As a result, cross correlation shows higher variation of shear-wave velocities between events than those of the deconvolution.
7. The predominant frequency derived from the average shear-wave velocity of the structure is 15% greater than that computed from the CMIF. This difference is plausible because the simple formula ($f = V_s/4H$, in which H is the total height) used to derive the frequencies does not consider any bending deformation (Ebrahimian and

Table 6

Mean Slope of Different Layers, Quality Factor Q , and Intrinsic-Damping Ratio ξ (in Percentage) Computed for Different Earthquakes

Event	East–West			North–South		
	Slope	Q	ξ (%)	Slope	Q	ξ (%)
1	−0.11	13.6	3.7	−0.11	16.2	3.1
2	−0.10	14.7	3.4	−0.10	16.3	3.1
3	−0.12	12.1	4.1	−0.14	12.3	4.1
4	−0.11	13.1	3.8	−0.12	13.1	3.8
5	−0.09	15.1	3.3	−0.09	16.2	3.1
Average		13.7	3.7		14.8	3.4

Todorovska, 2014) and assumes that the building's response is pure shear.

8. The damping ratio identified by the deconvolution is consistent for five earthquakes. The average intrinsic-damping ratio is found to be 3.5% in the translational directions. We interpret the damping as that of the structure because rocking for that building was immaterial.
9. It is shown that both deconvolution and cross-correlation methods can be used to perform propagating-wave-based system identification of buildings to complement modal-based methods, which is of key importance for performance assessment of structures before and after earthquakes. Predictions of structural motion calculated from IRFs convolved with previously observed weak-to-moderate ground-motion time histories could lead to predictions of the onset of nonlinear action.

Data and Resources

Instruments of the National Strong Motion Network of U.S. Geological Survey collected recordings were used in this study. The records from the 22 June 2009 (M 5.4) and 25 September 2014 (M 6.2) earthquakes can be downloaded from <http://www.strongmotioncenter.org/> (last accessed November 2016). The records from the 6 April 2005 (M 4.9), 27 July 2006 (M 4.7) and 20 September 2010 (M 4.9) earthquakes are available from the National Strong Motion Project (GS-G-WR_ESC_NSMP@usgs.gov) upon request. Figure 4 is modified from <http://earthquake.usgs.gov/monitoring/nsmp/structures/img/schematics/8040.pdf> (last accessed November 2016). In Figure 5, the fault lines were obtained from <http://www.dggs.alaska.gov/pubs/id/24956> (last accessed November 2016), which included fault information from Koehler *et al.* (2012, 2013). The MATLAB version of the complex mode indicator function used in this study is available at <http://www.mathworks.com/matlabcentral/fileexchange/59943-cmif-complex-mode-indication-function> (last accessed November 2016). The unpublished manuscript by E. Kalkan, H. S. Ulusoy, W. Wen, J. P. B. Fletcher, F. Wang, and N. Nakata (2017), "Site properties inferred at Delaney Park downhole array in Anchorage Alaska," accepted for publication in *Bull. Seismol. Soc. Am.*

Acknowledgments

We would like to thank Maria Todorovska, Nori Nakata, Brad Aagaard, and an anonymous reviewer for thorough reviews, which helped to improve the technical quality and presentation of this article. Special thanks are extended to Christopher Stephens for providing the waveform data, Luke Blair for preparing the regional earthquake fault maps, Shahneam Reza and Timothy Cheng for drafting the sensor layout, and Fei Wang for illustrating the shear-wave velocity profile. We also thank Joe Fletcher and Nori Nakata for fruitful discussions on deconvolution and cross correlation, and for sharing their computer codes, which we modified significantly for this study. Last but not least, we would like to thank U.S. Geological Survey's National Strong Motion Network technicians James Smith, Jonah Merritt, and Jason De Cristofaro for keeping the Atwood Building seismic array up and running. China Scholarship Council provided the financial support for Weiping Wen.

References

- Aki, K. (1957). Space and time spectra of stationary stochastic waves, with special reference to microtremors, *Bull. Earthq. Res. Inst.* **35**, 415–456.
- Aki, K., and P. G. Richards (2002). *Quantitative Seismology*, University Science Books, Mill Valley, California.
- Allemang, R. J. (2003). The modal assurance criterion—Twenty years of use and abuse, *Sound Vib.* **37**, no. 8, 14–23.
- Allemang, R. J., and D. L. Brown (1982). A correlation coefficient for modal vector analysis, *1st International Modal Analysis Conference*, Vol. 1, SEM, Orlando, Florida, 110–116.
- Allemang, R. J., and D. L. Brown (2006). A complete review of the complex mode indicator function (CMIF) with applications, *Proc. of ISMA2006 International Conference on Noise and Vibration Engineering*, Leuven, Belgium, 3209–3246.
- Boore, D. M. (2004). Ground motion in Anchorage, Alaska, from the 2002 Denali fault earthquake: Site response and displacement pulses, *Bull. Seismol. Soc. Am.* **94**, no. 6, 72–84.
- Boutin, C., S. Hans, E. Ibraim, and P. Roussillon (2005). In situ experiments and seismic analysis of existing buildings. Part II: Seismic integrity threshold, *Earthq. Eng. Struct. Dynam.* **34**, 1531–1546.
- Bruhn, R. L. (1979). Holocene displacements measured by trenching the Castle Mountain fault near Houston, Alaska, *Short notes on Alaskan geology—1978, Alaska Division of Geological and Geophysical Surveys Profess Report 112*, 1–9.
- Çelebi, M. (2006). Recorded earthquake responses from the integrated seismic monitoring network of the Atwood Building, Anchorage, Alaska, *Earthq. Spectra* **22**, no. 4, 847–864.
- Cheng, M. H., M. D. Kohler, and T. H. Heaton (2015). Prediction of wave propagation in buildings using data from a single seismometer, *Bull. Seismol. Soc. Am.* **105**, no. 1, 107–119.
- Ebrahimian, M., and M. I. Todorovska (2014). Wave propagation in a Timoshenko beam building model, *J. Eng. Mech.* **140**, no. 5, doi: [10.1061/\(ASCE\)EM.1943-7889.0000720](https://doi.org/10.1061/(ASCE)EM.1943-7889.0000720).
- Ebrahimian, M., and M. I. Todorovska (2015). Structural system identification of buildings by a wave method based on a nonuniform Timoshenko beam model, *J. Eng. Mech.* **141**, no. 8, doi: [10.1061/\(ASCE\)EM.1943-7889.0000933](https://doi.org/10.1061/(ASCE)EM.1943-7889.0000933).
- Finno, R. J., and D. G. Zapata-Medina (2014). Effects of construction-induced stresses on dynamic soil parameters of Bootlegger Cove Clays, *J. Geotech. Geoenviron. Eng.* **140**, no. 4, ID: 04013051.
- Fogelman, K., C. Stephens, J. C. Lahr, S. Helton, and M. Allen (1978). Catalog of earthquakes in southern Alaska, October–December, 1977, *U.S. Geol. Surv. Open-File Rept.* 78–1097.
- Ghanem, R., and M. Shinozuka (1995). Structural system identification—I: Theory, *J. Eng. Mech.* **121**, no. 2, 255–264.
- International Conference of Building Officials [ICBO] (1979). *Uniform Building Code*, Whittier, California.
- Iwan, W. D. (1997). Drift spectrum: Measure of demand for earthquake ground motions, *J. Struct. Eng.* **123**, 367–404.
- Kawakami, H., and M. Oyunchimeg (2004). Normalized input-output minimization analysis of earthquake wave propagation in damaged and undamaged buildings, *13th World Conference on Earthquake Engineering*, Vancouver, B.C., Canada, 1–6 August, Paper Number 3170.
- Koehler, R. D. (2013). *Quaternary Faults and Folds (QFF): Alaska Division of Geological & Geophysical Surveys Digital Data Series 3* Alaska Division of Geological & Geophysical Surveys, Fairbanks, Alaska.
- Koehler, R. D., R.-E. Farrell, P. A. C. Burns, and R. A. Combellick (2012). Quaternary faults and folds in Alaska: A digital database, 31 pp., 1 sheet, 1:3,700,000.
- Kohler, M. D., T. H. Heaton, and S. C. Bradford (2007). Propagating waves in the steel, moment-frame factor building recorded during earthquakes, *Bull. Seismol. Soc. Am.* **97**, no. 4, 1334–1345.
- Lade, P. V., R. G. Updike, and D. A. Cole (1988). Cyclic triaxial tests of the Bootlegger Cove formation, Anchorage, Alaska, *U.S. Geol. Surv. Bull.* **1825**, 51 pp.

- Lahr, J. C., R. A. Page, C. D. Stephens, and K. A. Fogleman (1986). Sutton, Alaska, earthquake of 1984—Evidence for activity on the Talkeetna segment of the Castle Mountain fault system, *Bull. Seismol. Soc. Am.* **76**, no. 4, 967–983.
- Larose, E., L. Margerin, A. Derode, B. van Tiggelen, M. Campillo, N. Shapiro, A. Paul, L. Stehly, and M. Tanter (2006). Correlation of random wave fields: An interdisciplinary review, *Geophysics* **71**, no. 4, SI11–SI21.
- Li, J., G. A. Abers, Y. Kim, and D. Christensen (2013). Alaska megathrust 1: Seismicity 43 years after the great 1964 Alaska megathrust earthquake, *J. Geophys. Res.* **118**, no. 9, 4861–4871.
- Mehta, K., R. Snieder, and V. Grazier (2007a). Extraction of near-surface properties for a lossy layered medium using the propagator matrix, *Geophys. J. Int.* **169**, 271–280.
- Mehta, K., R. Snieder, and V. Grazier (2007b). Downhole receiver function: A case study, *Bull. Seismol. Soc. Am.* **97**, 1396–1403.
- Nakata, N., and R. Snieder (2014). Monitoring a building using deconvolution interferometry. II: Ambient-vibration analysis, *Bull. Seismol. Soc. Am.* **104**, no. 1, 204–213.
- Nakata, N., R. Snieder, S. Kuroda, S. Ito, T. Aizawa, and T. Kunimi (2013). Monitoring a building using deconvolution interferometry. I: Earthquake-data analysis, *Bull. Seismol. Soc. Am.* **103**, no. 3, 1662–1678.
- Nakata, N., W. Tanaka, and Y. Oda (2015). Damage detection of a building caused by the 2011 Tohoku-Oki earthquake with seismic interferometry, *Bull. Seismol. Soc. Am.* **105**, 2411–2419.
- Nath, S. K., D. Chatterjee, N. N. Biswas, M. Dravinski, D. A. Cole, A. Papageorgiou, J. A. Rodriguez, and C. J. Poran (1997). Correlation study of shear-wave velocity in near surface geological formations in Anchorage, Alaska, *Earthq. Spectra* **13**, no. 1, 55–75.
- Newton, C., and R. Snieder (2012). Estimating intrinsic attenuation of a building using deconvolution interferometry and time reversal, *Bull. Seismol. Soc. Am.* **102**, no. 5, 2200–2208.
- Oth, A., S. Parolai, and D. Bindi (2011). Spectral analysis of K-NET and KiK-net data in Japan, Part I: Database compilation and peculiarities, *Bull. Seismol. Soc. Am.* **101**, no. 2, 652–666.
- Pandey, A. K., M. Biswas, and M. M. Samman (1991). Damage detection from changes in curvature mode shapes, *J. Sound Vib.* **145**, no. 2, 321–332.
- Parolai, S., A. Ansal, A. Kurtulus, A. Strollo, R. Wang, and J. Zschau (2009). The Ataköy vertical array (Turkey): Insights into seismic wave propagation in the shallow-most crustal layers by waveform, *Geophys. J. Int.* **178**, 1649–1662.
- Parolai, S., D. Bindi, A. Ansal, A. Kurtulus, A. Strollo, and J. Zschau (2010). Determination of shallow S-wave attenuation by down-hole waveform deconvolution: A case study in Istanbul (Turkey), *Geophys. J. Int.* **181**, no. 2, 1147–1158.
- Pastor, M., M. Binda, and T. Harčarik (2012). Modal assurance criterion, *Procedia Eng.* **48**, 543–548.
- Petrovic, B., and S. Parolai (2016). Joint deconvolution of building and downhole strong-motion recordings: Evidence for the seismic wave-field being radiated back into the shallow geological layers, *Bull. Seismol. Soc. Am.* **106**, no. 4, doi: [10.1785/0120150326](https://doi.org/10.1785/0120150326).
- Picozzi, M. (2012). An attempt of real-time structural response assessment by an interferometric approach: A tailor-made earthquake early warning for buildings, *Soil Dynam. Earthq. Eng.* **38**, 109–118.
- Picozzi, M., S. Parolai, M. Mucciarelli, C. Milkereit, D. Bindi, R. Ditommaso, M. Vona, M. R. Gallipoli, and J. Zschau (2011). Interferometric analysis of strong ground motion for structural health monitoring: The example of the L'Aquila, Italy, seismic sequence of 2009, *Bull. Seismol. Soc. Am.* **101**, no. 2, 635–651.
- Plafker, G., L. M. Gilpin, and J. C. Lahr (1994). Neotectonic map of Alaska, in *The Geology of Alaska*, G. Plafker and H. C. Berg (Editors), Geol. Soc. Am., Boulder, Colorado, Vol. G-1, 389–449.
- Prieto, G. A., J. F. Lawrence, A. I. Chung, and M. D. Kohler (2010). Impulse response of civil structures from ambient noise analysis, *Bull. Seismol. Soc. Am.* **100**, no. 5A, 2322–2328.
- Rades, M. (2010). Performance of various mode indicator functions, *Shock Vib.* **17**, 473–482.
- Rahmani, M., and M. I. Todorovska (2013). 1D system identification of buildings from earthquake response by seismic interferometry with waveform inversion of impulse responses—Method and application to Millikan Library, *Soil Dynam. Earthq. Eng.* **47**, 157–174.
- Rahmani, M., and M. I. Todorovska (2015). Structural health monitoring of a 54-story steel-frame building using a wave method and earthquake records, *Earthq. Spectra* **31**, no. 1, 501–525.
- Rahmani, M., M. Ebrahimian, and M. I. Todorovska (2015a). Wave dispersion in high-rise buildings due to soil-structure interaction, *Earthq. Eng. Struct. Dynam.* **44**, 317–323.
- Rahmani, M., M. Ebrahimian, and M. I. Todorovska (2015b). Time-wave velocity analysis for early earthquake damage detection in buildings: Application to a damaged full-scale RC building, *Earthq. Eng. Struct. Dynam.* **44**, no. 4, 619–636.
- Roux, P., P. Guéguen, L. Baillet, and A. Hamze (2014). Structural-change localization and monitoring through a perturbation-based inverse problem, *J. Acoust. Soc. Am.* **136**, no. 5, 2586–2597, doi: [10.1121/1.4897403](https://doi.org/10.1121/1.4897403).
- Sabra, K. G., P. Gerstoft, P. Roux, W. A. Kuperman, and M. C. Fehler (2005). Extracting time-domain Green's function estimates from ambient seismic noise, *Geophys. Res. Lett.* **32**, no. 3, doi: [10.1029/2004GL021862](https://doi.org/10.1029/2004GL021862).
- Schuster, G. T. (2009). *Seismic Interferometry*, Cambridge University Press, Cambridge, Massachusetts, 30–50.
- Schuster, G. T., J. Yu, J. Sheng, and J. Rickett (2004). Interferometric/daylight seismic imaging, *Geophys. Res. Lett.* **157**, no. 2, 838–852.
- Shih, C. Y., Y. G. Tsuei, R. J. Allemang, and D. L. Brown (1988). Complex mode indication function and its applications to spatial domain parameter estimation, *Mech. Syst. Signal Process.* **2**, no. 4, 367–377.
- Smart, K. J., T. L. Pavlis, V. B. Sisson, S. M. Roeske, and L. W. Snee (1996). The Border Ranges fault system in Glacier Bay National Park, Alaska: Evidence for major early Cenozoic dextral strike-slip motion, *Can. J. Earth Sci.* **33**, no. 9, 1268–1282.
- Snieder, R. (2004). Extracting the Green's function from the correlation of coda waves: A derivation based on stationary phase, *Phys. Rev. E* **69**, no. 4, 046610.
- Snieder, R. (2007). Extracting the Green's function of attenuating heterogeneous acoustic media from uncorrelated waves, *J. Acoust. Soc. Am.* **121**, no. 5, 2637–2643.
- Snieder, R., and E. Şafak (2006). Extracting the building response using seismic interferometry: Theory and application to the Millikan library in Pasadena, California, *Bull. Seismol. Soc. Am.* **96**, no. 2, 586–598.
- Snieder, R., M. Miyazawa, E. Slob, I. Vasconcelos, and K. Wapenaar (2009). A comparison of strategies for seismic interferometry, *Surv. Geophys.* **30**, nos. 4/5, 503–523.
- Snieder, R., J. Sheiman, and R. Calvert (2006). Equivalence of the virtual-source method and wave-field deconvolution in seismic interferometry, *Phys. Rev. E* **73**, 066620.
- Steidl, J. H. (2006). Inventory of existing strong-motion geotechnical arrays, *Proc. of the International Workshop for International Workshop for Site Selection, Installation, and Operation of Geotechnical Strong-Motion Arrays Workshop 2: Guidelines for Installation, Operation, and Data Archiving and Dissemination*, La Jolla, California, Cosmos Publication Number CP-2006/01.
- Todorovska, M. I. (2009). Seismic interferometry of a soil-structure interaction model with coupled horizontal and rocking response, *Bull. Seismol. Soc. Am.* **99**, no. 2A, 611–625.
- Todorovska, M. I., and M. Rahmani (2012). Recent advances in wave travel time based methodology for structural health monitoring and early earthquake damage detection in buildings, *Proc. of the 15th World Conference on Earthquake Engineering*, 24–28.
- Todorovska, M. I., and M. D. Trifunac (2008). Impulse response analysis of the Van Nuys 7-story hotel during 11 earthquakes and earthquake damage detection, *Struct. Contr. Health Monit.* **15**, 90–116.

- Ulery, C. A., R. G. Updike, and USGS Office of Earthquakes, (1983). Subsurface structure of the cohesive facies of the Bootlegger Cove formation, southwest Anchorage: Alaska, *Div. Geol. Geophys. Surv. Profess. Rept. 84*, 5 p., 3 sheets, scale 1:15,840.
- Ulusoy, H. S., E. Kalkan, and K. Banga (2013). Real-time seismic monitoring of Veterans Affairs hospital buildings, *Proc. of the SPIE Smart Structures Conference*, San Diego, California.
- Updike, R. G., and B. A. Carpenter (1986). Engineering geology of the government hill area, Anchorage, Alaska, *U.S. Geol. Surv. Bull. 1588*, 36 pp.
- Updike, R. G., and C. A. Ulery (1986). Engineering-geologic map of southwest Anchorage, Alaska: Alaska, *Div. Geol. Geophys. Surv. Profess. Rept. 89*, 1 sheet, scale 1:15,840.
- Vasconcelos, I., and R. Snieder (2008). Interferometry by deconvolution: Part 1—Theory for acoustic waves and numerical examples, *Geophysics* **73**, no. 3, S115–S128.
- Wapenaar, K., D. Draganov, R. Snieder, X. Campman, and A. Verdel (2010). Tutorial on seismic interferometry: Part 1—Basic principles and applications, *Geophysics* **75**, no. 5, A195–A209.
- Wapenaar, K., J. Van Der Neut, E. Ruigrok, D. Draganov, J. Hunziker, E. Slob, J. Thorbecke, and R. Snieder (2011). Seismic interferometry by cross-correlation and by multidimensional deconvolution: A systematic comparison, *Geophys. J. Int.* **185**, no. 3, 1335–1364.
- Wong, I., T. Dawson, M. Dober, and Y. Hashash (2010). Evaluating the seismic hazard in Anchorage, Alaska, *Proc. of the 9th U.S. National and 10th Canadian Conference on Earthquake Engineering*, 25–29 July, Toronto, Ontario, Canada, Paper Number 785.
- Yang, Z., U. Dutpa, M. Çelebi, H. Liu, N. Biswas, T. Kono, and H. Benz (2004). Strong motion instrumentation and structural response of Atwood Building in downtown Anchorage, Alaska, *Proc. of the 13th World Conference on Earthquake Engineering*, Vancouver, B.C., Canada, 1–6 August 2004.
- Yang, Z., U. Dutta, F. Xiong, N. Biswas, and H. Benz (2008). Seasonal frost effects on the dynamic behavior of a twenty-story office building, *Cold Reg. Sci. Tech.* **51**, 76–84.

Key Lab of Structures Dynamic Behavior and Control of the Ministry of Education
Harbin Institute of Technology
Harbin 150090, China
wenweiping.hit@gmail.com
(W.W.)

Earthquake Science Center
U.S. Geological Survey
345 Middlefield Road MS 977
Menlo Park, California 94025
ekalkan@usgs.gov
(E.K.)

Manuscript received 2 March 2016